



## Coulomb excitation of $\text{Zn}^{74,76}$

A. Illana, M. Zielińska, M. Huyse, E. Rapisarda, P. van Duppen, K. Wrzosek-Lipska, S M Lenzi, F. Nowacki, D D Dao, T. Otsuka, et al.

### ► To cite this version:

A. Illana, M. Zielińska, M. Huyse, E. Rapisarda, P. van Duppen, et al.. Coulomb excitation of  $\text{Zn}^{74,76}$ . Physical Review C, 2023, 108 (4), pp.044305. 10.1103/physrevc.108.044305 . hal-04291573

**HAL Id: hal-04291573**

**<https://hal.science/hal-04291573>**

Submitted on 17 Nov 2023

**HAL** is a multi-disciplinary open access archive for the deposit and dissemination of scientific research documents, whether they are published or not. The documents may come from teaching and research institutions in France or abroad, or from public or private research centers.

L'archive ouverte pluridisciplinaire **HAL**, est destinée au dépôt et à la diffusion de documents scientifiques de niveau recherche, publiés ou non, émanant des établissements d'enseignement et de recherche français ou étrangers, des laboratoires publics ou privés.



Distributed under a Creative Commons Attribution 4.0 International License

Coulomb excitation of  $^{74,76}\text{Zn}$ 

A. Illana<sup>1,2,3</sup>, M. Zielińska<sup>4</sup>, M. Huyse<sup>1</sup>, E. Rapisarda<sup>5</sup>, P. Van Duppen<sup>1</sup>, K. Wrzosek-Lipska<sup>6</sup>, S. M. Lenzi<sup>7</sup>,  
 F. Nowacki<sup>8</sup>, D. D. Dao<sup>8</sup>, T. Otsuka<sup>9</sup>, Y. Tsunoda<sup>10,11</sup>, K. Arnsward<sup>12</sup>, M. J. G. Borge<sup>13</sup>,  
 J. Cederkäll<sup>14</sup>, K. Chrysalidis<sup>13,15</sup>, M. L. Cortés<sup>16,17</sup>, D. M. Cox<sup>3,18</sup>, T. Day Goodacre<sup>13,19</sup>, H. De Witte<sup>1</sup>,  
 D. T. Doherty<sup>4,20</sup>, V. Fedosseev<sup>13</sup>, L. P. Gaffney<sup>21</sup>, K. Hadyńska-Klęk<sup>2</sup>, H. Hess<sup>12</sup>, C. Henrich<sup>16</sup>, M. Hlebowicz<sup>22,6</sup>,  
 M. Komorowska<sup>4,6</sup>, W. Korten<sup>4</sup>, Th. Kröll<sup>16</sup>, M. L. Lozano Benito<sup>13</sup>, R. Lutter<sup>23</sup>, B. Marsh<sup>13</sup>, L. Martikainen<sup>13</sup>,  
 M. Matejska-Minda<sup>6,24</sup>, P. L. Molkanov<sup>25</sup>, E. Nacher<sup>26</sup>, A. Nannini<sup>27</sup>, P. J. Napiorkowski<sup>6</sup>, J. Pakarinen<sup>3,18</sup>, P. Papadakis<sup>3,18</sup>,  
 M. Queiser<sup>12</sup>, P. Reiter<sup>12</sup>, M. Rocchini<sup>27</sup>, J. A. Rodriguez<sup>13</sup>, T. Rolke<sup>12</sup>, D. Rosiak<sup>12</sup>, S. Rothe<sup>13</sup>, M. Seidlitz<sup>12</sup>, C. Seiffert<sup>13</sup>,  
 B. Siebeck<sup>12</sup>, E. Siesling<sup>13</sup>, J. Snäll<sup>13,14</sup>, J. Srebrny<sup>6</sup>, S. Thiel<sup>12</sup>, N. Warr<sup>12</sup> and F. Wenander<sup>13</sup>

(ISOLDE Collaboration)

<sup>1</sup>KU Leuven, Instituut voor Kern- en Stralingsfysica, B-3001 Leuven, Belgium<sup>2</sup>Istituto Nazionale di Fisica Nucleare, Laboratori Nazionali di Legnaro, I-35020 Legnaro, Italy<sup>3</sup>Accelerator Laboratory, Department of Physics, University of Jyväskylä, FI-40014 Jyväskylä, Finland<sup>4</sup>Ifu, CEA, Université Paris-Saclay, F-91191 Gif-sur-Yvette, France<sup>5</sup>Paul Scherrer Institute, CH-5232 Villigen PSI, Switzerland<sup>6</sup>Heavy Ion Laboratory, University of Warsaw, PL-02-093 Warsaw, Poland<sup>7</sup>Dipartimento di Fisica e Astronomia, Università di Padova and INFN Sezione di Padova, I-35131 Padova, Italy<sup>8</sup>Université de Strasbourg, CNRS, IPHC UMR 7178, F-67000 Strasbourg, France<sup>9</sup>Department of Physics, The University of Tokyo, 7-3-1 Hongo, Bunkyo, Tokyo 113-0033, Japan<sup>10</sup>Center for Computational Sciences, University of Tsukuba, 1-1-1 Tennodai, Tsukuba, Ibaraki 305-8577, Japan<sup>11</sup>Center for Nuclear Study, The University of Tokyo, 7-3-1 Hongo, Bunkyo, Tokyo 113-0033, Japan<sup>12</sup>Institut für Kernphysik, Universität zu Köln, Köln D-50937, Germany<sup>13</sup>CERN, CH-1211 Geneva 23, Switzerland<sup>14</sup>Physics Department, University of Lund, Box 118, SE-221 00 Lund, Sweden<sup>15</sup>Institut für Physik, Johannes Gutenberg-Universität, Mainz D-55099, Germany<sup>16</sup>Institut für Kernphysik, Technische Universität Darmstadt, D-64289 Darmstadt, Germany<sup>17</sup>GSI Helmholtzzentrum für Schwerionenforschung, D-64291 Darmstadt, Germany<sup>18</sup>Helsinki Institute of Physics, University of Helsinki, P.O. Box 64, FI-00014 Helsinki, Finland<sup>19</sup>School of Physics and Astronomy, The University of Manchester, Manchester M13 9PL, United Kingdom<sup>20</sup>Department of Physics, University of York, Heslington, York YO10 5DD, United Kingdom<sup>21</sup>School of Engineering, University of the West of Scotland, Paisley PA1 2BE, United Kingdom<sup>22</sup>Warsaw University of Technology, PL-00-662 Warsaw, Poland<sup>23</sup>Fakultät für Physik, Ludwig-Maximilians-Universität München, D-85740 Garching, Germany<sup>24</sup>Institute of Nuclear Physics Polish Academy of Sciences, PL-31342 Cracow, Poland<sup>25</sup>Petersburg Nuclear Physics Institute, NRC Kurchatov Institute, 188300 Gatchina, Russia<sup>26</sup>Instituto de Estructura de la Materia, CSIC, E-28006 Madrid, Spain<sup>27</sup>Istituto Nazionale di Fisica Nucleare, Sezione di Firenze, I-50019 Sesto Fiorentino (Firenze), Italy

(Received 24 August 2022; revised 27 June 2023; accepted 26 July 2023; published 10 October 2023)

The first experiment using radioactive beams post-accelerated by the HIE-ISOLDE facility has enabled to obtain a precise set of  $B(E2)$  transition probabilities in neutron-rich  $^{74,76}\text{Zn}$  isotopes. The resulting  $B(E2; 2_1^+ \rightarrow 0_1^+)$  values are consistent with those determined in earlier REX-ISOLDE measurements. While the  $B(E2; 4_1^+ \rightarrow 2_1^+)$  transition probability in  $^{76}\text{Zn}$  is also in agreement with earlier Coulomb-excitation results, the value obtained for  $^{74}\text{Zn}$  is considerably lower. For the first time, a spectroscopic quadrupole moment of the  $2_1^+$  state was measured for an exotic nucleus in this mass region. A detailed comparison is presented with large-scale shell-model and Monte Carlo shell-model calculations.

DOI: [10.1103/PhysRevC.108.044305](https://doi.org/10.1103/PhysRevC.108.044305)

## I. INTRODUCTION

The region around the doubly magic nucleus  $^{78}\text{Ni}$ , with the  $Z = 28$  and  $N = 50$  shell closures, is particularly interesting for testing the validity of contemporary nuclear models and for unraveling new aspects of the interactions used in these models (see, e.g., Refs. [1–5]). In particular, the evolution of single-particle and collective phenomena between the harmonic oscillator shell closures at  $N = 40$  and the spin-orbit shell closure at  $N = 50$  challenges our understanding of nuclear structure [6]. In this region the transition from the harmonic oscillator to the spin-orbit shell closure is manifested and the neutron  $g_{9/2}$  orbital plays a crucial role in this process [1–7].

Recently, large-scale shell-model calculations predicted the appearance of shape coexistence in  $^{78}\text{Ni}$  and its link to a new island of inversion around  $^{74}\text{Cr}$  [8], similar to that observed around  $^{64}\text{Cr}$  [9]. The shell evolution [6,10] and the shape coexistence driven by type-II shell evolution [5,7] have been experimentally identified in the Ni and Cu isotopes as consequences of the varying occupation of the neutron  $g_{9/2}$  orbital, not only in lighter isotopes [11–20] but also in heavier Cu isotopes towards  $N = 50$  [21,22]. In fact, the data for the lowest states of  $^{77,79}\text{Cu}$  seem to suggest that their neutron shell structure is dominated by the filling scheme with the closed  $pf$  shell and valence neutrons in the  $g_{9/2}$  orbital. Even though some evidence of core excitations has been observed in the region [23], to first order the  $f_{7/2}$  orbital in the proton shell is almost fully occupied, and the proton  $p_{3/2}$  and  $f_{5/2}$  orbitals are nearly degenerate due to the shell evolution, favoring the development of collectivity. The shapes of the nuclei with  $N = 46$ –48 are sensitive to this scenario, and experimental data related to them help us to understand the structure evolution up to  $^{78}\text{Ni}$ .

Low-lying states of  $^{78}\text{Ni}$ , observed in Ref. [24], were interpreted as belonging to two distinct configurations, a spherical and a deformed one, in accordance with the results of conventional large-scale shell-model and Monte Carlo shell-model calculations [24]. However, the progression towards the most exotic systems around  $^{78}\text{Ni}$  demands detailed measurements to reveal their structures, probe the reliability of theoretical calculations and provide a more robust basis to extrapolate to the yet unexplored region. The collectivity of the Zn isotopes with  $N = 46$ –48 is expected to appear more distinctly. Moreover, contrary to the more exotic nuclei, they offer the possibility to measure electromagnetic properties of excited states, such as transition probabilities and quadrupole moments, with good precision.

In this paper we present the results on the electromagnetic structure of  $^{74,76}\text{Zn}$  obtained using low-energy Coulomb excitation in the first experiment performed at HIE-ISOLDE. Section II summarizes recent experimental results on heavy Zn nuclei. In Sec. III the experimental setup is introduced, and the properties of the beams used in the experiment are discussed. The data analysis and the extraction of electromagnetic matrix elements using the GOSIA code are presented in Sec. IV. The experimental results are compared with those obtained in previous measurements, as well as with the theoretical predictions, in Sec. V.

## II. RECENT EXPERIMENTAL RESULTS ON HEAVY Zn NUCLEI

The fragility of the  $N = 40$  subshell gap is reflected by the developing collectivity in the neutron-rich Zn isotopes. Unlike in the Ni isotopic chain, where a sharp peak in the  $2_1^+$  energy is observed for the  $N = 40$   $^{68}\text{Ni}$ , the  $2_1^+$  level in the  $Z = 30$  Zn nuclei slowly decreases in energy from 1077 keV at  $N = 38$  to the minimum of 599 keV at  $^{76}\text{Zn}$ , see Fig. 1. The sudden increase of the  $2_1^+$  energy observed for  $^{80}\text{Zn}$  [30] is consistent with a strong shell closure at  $N = 50$ . This is further supported by the energy of the  $4_1^+$  state in this nucleus, recently identified using proton knockout [27], corresponding to a sharp decrease of the  $E(4_1^+)/E(2_1^+)$  ratio,  $R_{4/2}$ , to a value of 1.31(2), far from what is expected for collective nuclei. The systematics of low-lying states in even-even Zn has recently been extended beyond  $N = 50$ , with the  $2_1^+$  and  $4_1^+$  states in  $^{82,84}\text{Zn}$  identified using in-beam  $\gamma$ -ray spectroscopy following proton knockout [28], and the measured excitation energies show that collectivity sets in rapidly when moving from  $N = 50$  towards heavier nuclei in the Zn isotopic chain.

The  $R_{4/2}$  are remarkably constant for all Zn isotopes from  $^{66}\text{Zn}$  to  $^{84}\text{Zn}$ , with the above-mentioned exception of  $^{80}\text{Zn}$ . Their values fall in between those predicted by two simple collective models:  $R_{4/2} = 2$  for spherical vibrators and 2.5 for  $\gamma$ -soft nuclei (Wilets-Jean model [31]). Indeed, the  $0_2^+$ ,  $2_2^+$ ,  $4_1^+$  states at roughly twice the energy of the  $2_1^+$  state are observed in  $^{66}\text{Zn}$  and  $^{72}\text{Zn}$ , see Fig. 1. However, the  $0_2^+$  state in  $^{68,70}\text{Zn}$  appears much lower in energy, closer to the  $2_1^+$  state than to  $4_1^+$ . It seems, in fact, that the energy of the  $0_2^+$  states in the  $^{66,68,70,72,74}\text{Zn}$  nuclei follows a parabolic trend as a function of neutron number between two closed shells at  $N = 28$  and 50, characteristic for intruder configurations. This interpretation is consistent with the results of multistep Coulomb-excitation studies of  $^{66,68}\text{Zn}$  [32–34] that show weak coupling of the  $0_2^+$  states to those below, and suggest that their structure may be influenced by the excitation to the  $\nu 1g_{9/2}$ , in contrast to other low-lying states in these isotopes. Consequently, it is more likely that the  $0_2^+$  states in Zn isotopes result from multiparticle-multihole excitations rather than being members of vibrational triplets. Removing the  $0_2^+$  states from consideration, the positions of the  $4_1^+$  and  $2_2^+$  states in all Zn isotopes from  $^{66}\text{Zn}$  to  $^{74}\text{Zn}$  are approximately consistent with what is expected for  $\gamma$ -soft nuclei. The recent identification of collective states built on the  $0_2^+$  and  $2_2^+$  band heads in  $^{74}\text{Zn}$  [29] further supports the role of the triaxial degree of freedom and configuration coexistence in the heavy Zn nuclei.

While excitation energies of low-lying excited states provide general information about the evolution of collectivity in an isotopic chain, more insight can be gained from measuring the transition probabilities and static electromagnetic moments. The systematics of  $g$  factors of the  $2_1^+$  states in even-even Zn isotopes has recently been extended to  $^{72}\text{Zn}$  [35,36]. The values for  $^{64-72}\text{Zn}$  [25,36] fall along the  $g = Z/A$  line, as expected for collective nuclei. In particular, no indication of a structural change is observed for  $N = 40$   $^{70}\text{Zn}$ .

The transition probabilities between low-lying states of most stable Zn isotopes are reasonably well known

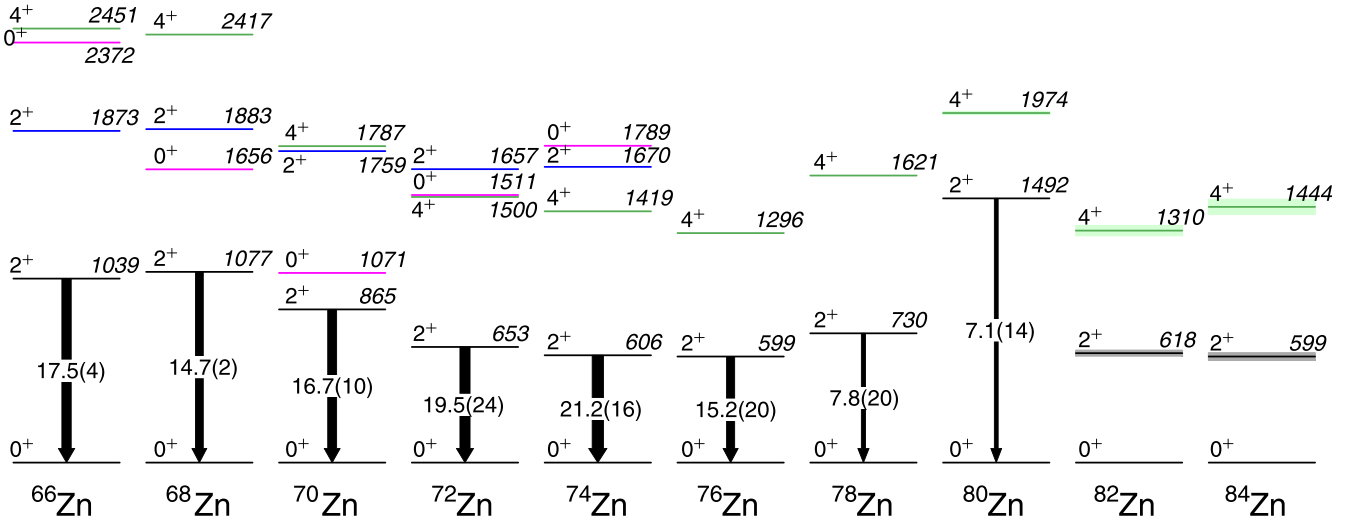


FIG. 1. Systematics of  $2^+$ ,  $4^+$ ,  $2^+$ , and  $0^+$  states and  $B(E2; 2^+ \rightarrow 0^+)$  values in even-even Zn isotopes from  $^{66}\text{Zn}$  ( $N = 36$ ) to  $^{84}\text{Zn}$  ( $N = 54$ ). Widths and labels of the arrows represent the measured  $B(E2; 2^+ \rightarrow 0^+)$  values, taken from ENSDF [25], with the exception of the values for  $^{76,78}\text{Zn}$  taken from Ref. [26], and expressed in Weisskopf units. Level energies, taken from ENSDF [25] and Refs. [27–29], are given in keV, and their uncertainties are plotted if they are larger than line width.

from multiple lifetime and Coulomb-excitation studies. The same experimental techniques were applied to neutron-rich Zn nuclei [26,27,30,37–44]. The  $B(E2; 2^+ \rightarrow 0^+)$  transition probabilities in  $^{72,74}\text{Zn}$  were measured using the recoil-distance method [40–42], low-energy [26,30,44] and intermediate-energy Coulomb excitation [37,38], and the obtained results are in good agreement. The low-energy Coulomb-excitation study [26,30] extended the  $B(E2; 2^+ \rightarrow 0^+)$  systematics in neutron-rich Zn isotopes to  $^{78,80}\text{Zn}$ , see Fig. 1. Similar to what is observed for the  $2^+$  energies, no effect of the  $N = 40$  subshell closure is visible, while the observed decrease of transition probabilities towards  $^{80}\text{Zn}$  is consistent with the strong shell closure at  $N = 50$ , in agreement with shell-model predictions using various model spaces and interactions [26,30].

Important discrepancies, however, are present between some of the  $B(E2; 4^+ \rightarrow 2^+)$  results obtained using different methods. Direct lifetime measurements [41,42] yielded  $B(E2; 4^+ \rightarrow 2^+)$  values in  $^{72,74}\text{Zn}$  that are consistently lower than those obtained in the Coulomb-excitation studies [26,30,44], with the difference of  $3\sigma$  observed for  $^{74}\text{Zn}$ . A similar disagreement is observed between the  $B(E2; 4^+ \rightarrow 2^+)$  values in  $^{70}\text{Zn}$  resulting from a Doppler-shift attenuation method (DSAM) study following low-energy Coulomb excitation [39] and the recoil-distance Doppler-shift (RDDS) measurements [41,42]. The origin of the systematic discrepancy between lifetime and Coulomb-excitation results is not understood and prevents firm conclusions on the structure of neutron-rich Zn nuclei. The present measurement was performed with the goal of providing new data with increased precision on the evolution of collectivity in the Zn isotopic chain.

### III. EXPERIMENT

The radioactive  $^{74,76}\text{Zn}$  nuclei were produced via fission induced by 1.4-GeV protons, accelerated by the PS-Booster at

CERN and impinging on a  $\text{UC}_x$  primary target. The reaction products diffused out of the heated target through a transfer line to the resonant ionization laser ion source (RILIS) [45]. The laser ionization process is highly selective, however other reaction products with a low ionization potential are surface ionized when passing through the hot cavity of RILIS, which led to the presence of isobaric gallium contaminants in the beam. After extraction from the ion source, the  $1^+$  ions were mass separated with the general purpose separator (GPS) prior to being injected into the Penning trap (REXTRAP) [46] for bunching and cooling. Subsequently, they were charge bred in the electron beam ion source (REXEBIS) [47] in preparation for post-acceleration. The charge-breeding time was 196 ms for  $^{76}\text{Zn}$  with a  $22^+$  charge state, while for  $^{74}\text{Zn}$  in the initial stage of the measurement it was equal to 496 ms, and later reduced to 96 ms with a change of the charge state from  $25^+$  to  $21^+$ .

The present experiment was the first to benefit from the increased energy of post-accelerated beams at ISOLDE. The previous post-acceleration system at ISOLDE, REX LINAC, was able to deliver beams with energy up to 2.9 MeV/nucleon. In 2015, the first superconducting cryomodule has been installed after the REX LINAC, increasing the available beam energy to 4.3 MeV/nucleon [48,49]. A slightly lower energy of 4.0 MeV/nucleon was used in the present experiment in order to maximize the excitation cross section, integrated over the scattering angles covered by the particle detector, for events corresponding to “safe” Coulomb excitation. In order to select the “safe” Coulomb-excitation events, the separation between the nuclear surfaces was required to be larger than 5 fm at the distance of the closest approach, as postulated by Ref. [50]. This condition assures that the influence of nuclear interactions on the observed population of excited states is negligible and consequently the well-established Coulomb-excitation theory can be used to relate the measured cross sections to electromagnetic

matrix elements. In order to enhance the differences between single- and multistep Coulomb excitation, measurements at 2.85 MeV/nucleon were performed as well.

The beam energies were determined using a Si detector that measured the energies of scattered beam particles, as described in detail in Ref. [51]. An upper limit of 0.7% was obtained for the full width at half-maximum (FWHM) relative to the centroid energy of the beam, which, for the 4.0 MeV/nucleon beams, translates into an uncertainty of 2 MeV on the incident beam energy of 296 MeV (for  $^{74}\text{Zn}$ ) and 304 MeV (for  $^{76}\text{Zn}$ ).

The  $\gamma$  rays depopulating Coulomb-excited states were detected in eight triple clusters of the Miniball array [52], working in coincidence with an annular, compact-disk (CD) shaped, double-sided silicon strip detector (DSSSD) [53] placed 23 mm downstream of the target and used for detection of scattered Zn projectiles and recoiling target nuclei. Efficiency calibration of Miniball was performed using standard  $^{152}\text{Eu}$  and  $^{133}\text{Ba}$  radioactive sources. The  $\gamma$ -ray efficiency at 1.3 MeV was measured to be 7.7%. The DSSSD consists of four identical quadrants, each of them subdivided into 24 radial sectors, coupled pairwise, and 16 annular strips. The detector covered an angular range from  $21^\circ$  to  $61^\circ$  in the laboratory frame, which corresponds in center of mass to  $28.8^\circ$ – $79^\circ$  for projectile detection in the DSSSD, and  $79^\circ$ – $138^\circ$  for recoil detection. All events with the scattered Zn nuclei detected in the DSSSD corresponded to the “safe” Coulomb-excitation process. The same is true for those with detection of target recoils at 2.85 MeV/nucleon beam energy, while at 4.0 MeV/nucleon the maximum center-of-mass scattering angle satisfying the criterion for “safe” Coulomb excitation [50] equals  $116^\circ$  and  $109^\circ$  for  $^{74}\text{Zn}$  and  $^{76}\text{Zn}$ , respectively. Consequently, events corresponding to the detection of recoils at laboratory angles lower than  $32.5^\circ$  for  $^{74}\text{Zn}$  ( $35.5^\circ$  for  $^{76}\text{Zn}$ ), i.e., in the three (four) innermost rings of the DSSSD, were excluded from the analysis.

Coulomb excitation of  $^{74,76}\text{Zn}$  was induced by two different targets:  $^{196}\text{Pt}$  of 2.0 mg/cm<sup>2</sup> thickness and  $^{208}\text{Pb}$ , 4.0 mg/cm<sup>2</sup> thick. The first one enabled the normalization of the measured Coulomb-excitation cross sections to the observed excitation of the  $^{196}\text{Pt}$  nuclei, in order to provide an independent measurement of the  $B(E2; 2_1^+ \rightarrow 0_1^+)$  transition probabilities. In contrast, the population of excited states in  $^{208}\text{Pb}$  was negligible under the present experimental conditions, and as a consequence possible  $\gamma$ -ray peaks due to the decay of states in  $^{74,76}\text{Zn}$  other than  $2_1^+$  and  $4_1^+$  would not be obscured by  $\gamma$  rays originating from the target nuclei. The total  $\gamma$ -ray spectra for  $^{74}\text{Zn}$  and  $^{76}\text{Zn}$  impinging on the  $^{208}\text{Pb}$  target are shown in Fig. 2. No transitions other than  $2_1^+ \rightarrow 0_1^+$  and  $4_1^+ \rightarrow 2_1^+$  were observed.

Figure 3 presents a comparison of  $\gamma$ -ray spectra observed for Coulomb excitation of the  $^{74}\text{Zn}$  beam on the  $^{196}\text{Pt}$  target measured at two beam energies with the same experimental conditions. Although the duration of the data collection with the 2.85 MeV/nucleon beam exceeded that for 4.0 MeV/nucleon by a factor of three, significantly higher statistics were collected for the low-energy transitions in  $^{74}\text{Ga}$  (171 keV) and  $^{196}\text{Pt}$  (336 keV) only. The number of counts in

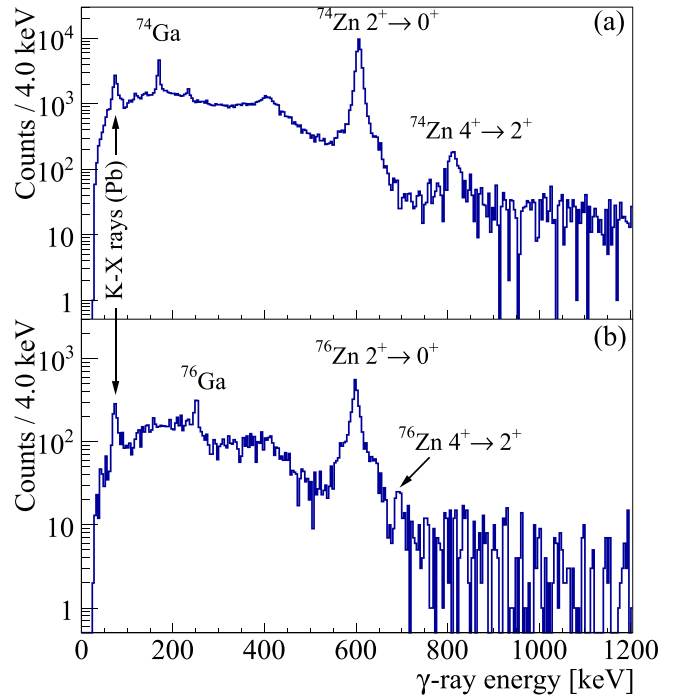


FIG. 2. Total  $\gamma$ -ray energy spectra for (a)  $^{74}\text{Zn}$  and (b)  $^{76}\text{Zn}$  impinging on  $^{208}\text{Pb}$  at 4.0 MeV/nucleon, background-subtracted and Doppler-corrected for the projectile. The “safe” energy criterion was imposed on the selection of the events, see text for details.

the  $2_1^+ \rightarrow 0_1^+$  transition in  $^{74}\text{Zn}$  (606 keV) is approximately equal for both spectra, illustrating the important gain in cross section for one-step Coulomb excitation of states at higher excitation energy that has been obtained due to the increase of beam energy. The gain is more evident for the two-step

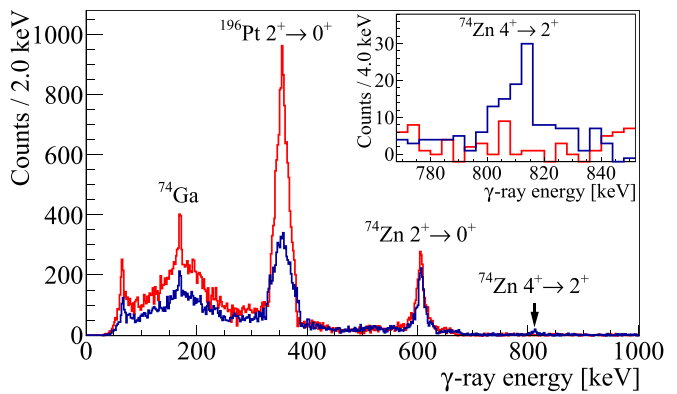


FIG. 3. Background-subtracted  $\gamma$ -ray spectra for  $^{74}\text{Zn}$  impinging on a  $^{196}\text{Pt}$  target, Doppler-corrected for the projectile. The spectrum plotted in blue was collected for a duration of 5 h at the beam energy of 4.0 MeV/nucleon. A spectrum obtained under the same experimental conditions, but at 2.85 MeV/nucleon and during 16 h of data collection is presented in red. The inset shows the 770–850 keV portions of the spectra, evidencing the enhancement of the  $4_1^+ \rightarrow 2_1^+$  transition at 4.0 MeV/nucleon. The “safe” energy criterion was imposed, see text for details.



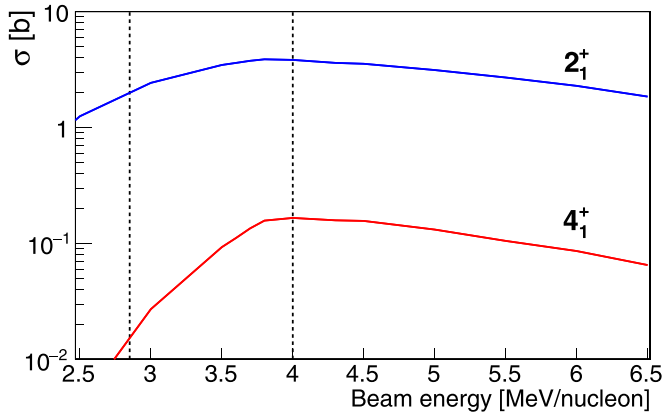


FIG. 4. Cross sections for Coulomb excitation of the  $2_1^+$  and  $4_1^+$  states in  $^{74}\text{Zn}$  on  $^{208}\text{Pb}$ , calculated as a function of the beam energy assuming the values of matrix elements obtained in the present work. The integration was performed over the scattering angles covered by the particle detector, excluding those corresponding to nonsafe Coulomb-excitation process (see text for details). Dashed lines indicate the beam energies used in the present experiment.

excitation of the  $4_1^+$  state in  $^{74}\text{Zn}$ , which is almost negligible at 2.85 MeV/nucleon and prominent at 4.0 MeV/nucleon.

This is quantified in Fig. 4, which presents the cross sections for Coulomb excitation of the  $2_1^+$  and  $4_1^+$  states in  $^{74}\text{Zn}$  on  $^{208}\text{Pb}$ , calculated as a function of the beam energy, for the particle detection geometry of the present measurement. The calculations were performed using the GOSIA code [54,55] assuming the values of matrix elements obtained in the present work. At beam energies below 4 MeV/nucleon, the excitation cross section for the  $4_1^+$  state experiences a greater relative increase as a function of beam energy than that for the  $2_1^+$  state. In particular, when going from 2.85 MeV/nucleon to 4 MeV/nucleon, a gain of a factor of 8 is observed for the  $4_1^+$  state, as compared to a factor of 2 for the  $2_1^+$  state. The integration over scattering angles covered by the particle detector was limited to the events corresponding to “safe” Coulomb-excitation process, and thus a gradual decrease of cross sections is observed for beam energies above 4 MeV/nucleon.

The beam intensity measured upstream of Miniball was  $5 \times 10^6$  and  $10^6$  pps for  $^{74,76}\text{Zn}$ , respectively. This represents an enhancement of one order of magnitude as compared to the previous Coulomb-excitation measurement of  $^{74,76}\text{Zn}$  at REX-ISOLDE [26], achieved thanks to dedicated target-ion source developments [56,57]. The beam composition was monitored by performing regular measurements with the RILIS lasers periodically switched ON and OFF. Figure 5 shows a comparison of spectra acquired with and without laser ionization. The  $2_1^+ \rightarrow 0_1^+$  transition in  $^{74}\text{Zn}$  is not present in the spectrum collected with the lasers switched off. However, from the comparison it is evident that a substantial fraction of the observed  $2_1^+ \rightarrow 0_1^+$  intensity in  $^{196}\text{Pt}$  is related to its excitation by  $^{74}\text{Ga}$ . This has been taken into account when using the observed excitation of  $^{196}\text{Pt}$  to normalize the cross sections measured for  $^{74}\text{Zn}$ , as explained in Sec. IV A. No transitions from beam contaminants other than  $^{74}\text{Ga}$  are visible in the spectra.

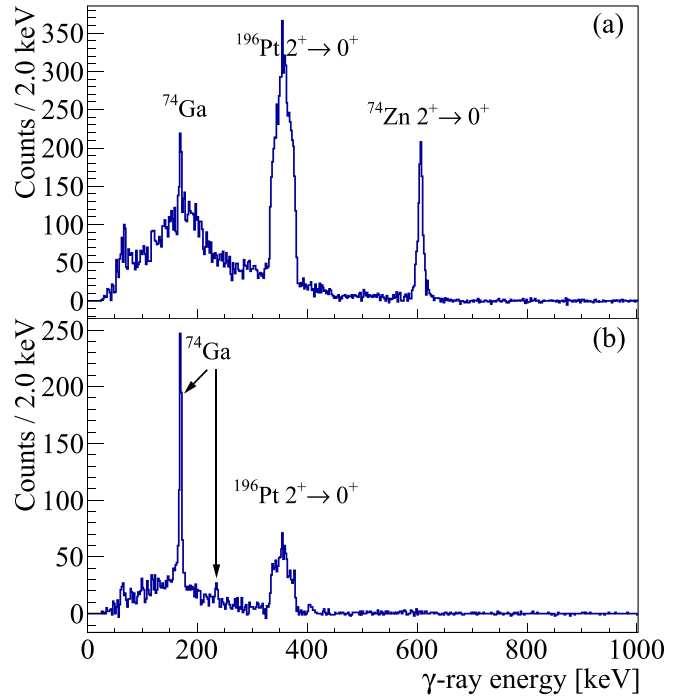


FIG. 5.  $\gamma$ -ray energy spectra for the  $A = 74$  beam impinging on  $^{196}\text{Pt}$  at 2.85 MeV/nucleon, background-subtracted and Doppler-corrected for the projectile. The spectrum in (a) was collected in laser ON mode, while that in (b) was collected during laser OFF periods.

From a comparison of the data collected in laser ON and OFF modes, the beam purity was estimated to be 90(2)% for  $^{74}\text{Zn}$  and 70(5)% for  $^{76}\text{Zn}$ , and in both cases the only contaminants observed were the Ga isobars. A similar beam composition was observed in the previous Coulomb-excitation measurement of  $^{74,76}\text{Zn}$  at ISOLDE (82(1)% purity for  $^{74}\text{Zn}$  and 79(2)% for  $^{76}\text{Zn}$  [26]).

The REX/HIE-ISOLDE facility provides a bunched exotic beam with a certain repetition rate and time duration. These numbers are dependent on the ion species, the beam intensity, and the optimal charge state for acceleration [58]. In the first experimental campaign with the HIE-ISOLDE accelerator, the choice of the time structure of the beam was limited due to the use of a temporary amplifier with limited capabilities for the last cavity of the REX LINAC (9GAP), which prevented us from using the EBIS slow extraction mode. A repetition rate of 5 Hz (10 Hz) for  $^{74}\text{Zn}$  ( $^{76}\text{Zn}$ ) and an EBIS bunch length of 200 ms was used. Within the 200- $\mu\text{s}$  bunch, the beam intensity was furthermore not constant, but had a strong time dependence, with 30% of the beam intensity concentrated in the first 10  $\mu\text{s}$ . Combined with the higher average beam intensity of  $5 \times 10^6$  pps for  $^{74}\text{Zn}$ , this led to an instantaneous rate higher than  $5 \times 10^9$  pps impinging on the target.

#### IV. DATA ANALYSIS

The  $^{74,76}\text{Zn}$  beam structure had a negative impact on the quality of the recorded data, as for most of the events particle multiplicity was higher than 1 for each CD quadrant. As a consequence, the standard time-gating procedure applied in

TABLE I. Literature values of matrix elements between the low-lying states in  $^{196}\text{Pt}$ , used in the normalization of the Coulomb-excitation cross sections measured for  $^{74,76}\text{Zn}$ .

Matrix element	Value [eb]	Ref.
$\langle 2_1^+ \  E2 \  0_1^+ \rangle$	1.172 (3)	[25]
$\langle 2_2^+ \  E2 \  2_1^+ \rangle$	1.356 (3)	[25]
$\langle 4_1^+ \  E2 \  2_1^+ \rangle$	1.911 (14)	[25]
$\langle 2_1^+ \  E2 \  2_1^+ \rangle$	0.82 (10)	[62]
$\langle 2_2^+ \  E2 \  2_2^+ \rangle$	-0.52 (20)	[62]
$\langle 4_1^+ \  E2 \  4_1^+ \rangle$	1.36 (16)	[62]

previous experiments with Miniball, see Ref. [52] for details, could not be used, as it did not allow making proper particle- $\gamma$  correlations. In order to overcome this problem, the timing information of the time-to-digital converter (TDC) modules were used to identify genuine multiplicity-one events and only those events were included in the analysis.

#### A. Determination of $E2$ matrix elements

The electromagnetic matrix elements between the observed states in  $^{74,76}\text{Zn}$  were extracted from the Coulomb-excitation data using the GOSIA code [54,55] and its version handling mutual excitation of collision partners, GOSIA2. The code calculates excitation cross sections for individual states for a given set of matrix elements and the scattering kinematics, defined by the particle detection geometry and the beam energy. The subsequent calculation of the  $\gamma$ -ray decay intensities takes into account effects such as internal conversion, angular distribution of  $\gamma$  rays and its attenuation related to the finite size of  $\gamma$ -ray detectors as well as to the deorientation effect during recoil in vacuum. In order to compare the calculated  $\gamma$ -ray intensities with those measured experimentally, the former are integrated over the range of scattering angles covered by the particle detectors, as well as over the range of incident energies due to the beam slowing down in the target material. A  $\chi^2$  fit is then performed, yielding a set of matrix elements that optimally reproduce the Coulomb-excitation data.

In order to extract electromagnetic matrix elements from Coulomb-excitation data, the measured  $\gamma$ -ray intensities have to be converted to absolute cross sections. The data collected with the  $^{196}\text{Pt}$  target were normalized to the observed excitation of target nuclei, which could be accurately described using the literature information on the electromagnetic structure of  $^{196}\text{Pt}$ , see Table I. The  $\langle 2_1^+ \| E2 \| 0_1^+ \rangle$  matrix elements in  $^{74,76}\text{Zn}$  determined in this way were, in turn, used to obtain the proper normalization of the data collected with the  $^{208}\text{Pb}$  target. To achieve this, an iterative GOSIA-GOSIA2 analysis was performed, as proposed in Ref. [59] and tested in Refs. [60,61]. In order to make use of the dependence of the Coulomb-excitation cross sections on the scattering angle, the data were subdivided into subsets corresponding to different angular ranges as listed in Tables II and III.

In the first step of the analysis, the  $\langle 2_1^+ \| E2 \| 0_1^+ \rangle$  and  $\langle 2_1^+ \| E2 \| 2_1^+ \rangle$  matrix elements were determined using GOSIA2

TABLE II. Yields of observed  $\gamma$ -ray transitions in  $^{74}\text{Zn}$  and target nuclei (without correction for  $\gamma$ -ray detection efficiency), following Coulomb excitation on  $^{196}\text{Pt}$  and  $^{208}\text{Pb}$  targets, as a function of center-of-mass scattering angle. The intensities measured for  $^{196}\text{Pt}$  result from excitation of this nucleus by  $^{74}\text{Zn}$  and  $^{74}\text{Ga}$ ; in the analysis, they were corrected for the  $^{74}\text{Zn}$  beam purity equal to 90(2)%. Beam energies are expressed in MeV/nucleon.

$E_{\text{beam}}$ Target	$\theta_{\text{c.m.}}$	Nucleus	Transition	Counts	Label
2.85 $^{196}\text{Pt}$	28.8°–44.3°	$^{74}\text{Zn}$	$2_1^+ \rightarrow 0_1^+$	1130 (50)	A
		$^{196}\text{Pt}$	$2_1^+ \rightarrow 0_1^+$	4630 (180)	
	44.3°–59.5°	$^{74}\text{Zn}$	$2_1^+ \rightarrow 0_1^+$	1550 (40)	B
		$^{196}\text{Pt}$	$2_1^+ \rightarrow 0_1^+$	5260 (100)	
	59.5°–79.0°	$^{74}\text{Zn}$	$2_1^+ \rightarrow 0_1^+$	2240 (50)	C
		$^{196}\text{Pt}$	$2_1^+ \rightarrow 0_1^+$	7800 (220)	
	79.0°–114.8°	$^{74}\text{Zn}$	$2_1^+ \rightarrow 0_1^+$	2060 (50)	D
		$^{196}\text{Pt}$	$2_1^+ \rightarrow 0_1^+$	7400 (210)	
	114.8°–138.0°	$^{74}\text{Zn}$	$2_1^+ \rightarrow 0_1^+$	1010 (40)	E
		$^{196}\text{Pt}$	$2_1^+ \rightarrow 0_1^+$	3750 (100)	
4.0 $^{208}\text{Pb}$	28.3°–61.8°	$^{74}\text{Zn}$	$2_1^+ \rightarrow 0_1^+$	$1.281 (12) \times 10^4$	A'
			$4_1^+ \rightarrow 2_1^+$	97 (16)	
	61.8°–78.2°	$^{74}\text{Zn}$	$2_1^+ \rightarrow 0_1^+$	$9.73 (11) \times 10^3$	B'
			$4_1^+ \rightarrow 2_1^+$	270 (20)	
	78.2°–114.8°	$^{74}\text{Zn}$	$2_1^+ \rightarrow 0_1^+$	$6.58 (9) \times 10^3$	C'
			$4_1^+ \rightarrow 2_1^+$	300 (30)	
4.0 $^{196}\text{Pt}$	28.7°–108.1°	$^{74}\text{Zn}$	$2_1^+ \rightarrow 0_1^+$	730 (50)	D'
			$4_1^+ \rightarrow 2_1^+$	26 (10)	

from the data collected with the  $^{196}\text{Pt}$  target at 2.85 MeV/nucleon. The  $\gamma$ -ray intensities measured for  $^{196}\text{Pt}$ , listed in Tables II and III, were corrected for beam purity, determined from the laser ON/OFF measurements (see Sec. III). The level schemes for Zn nuclei, which were included in the calculations, were limited to the ground state and the  $2_1^+$  state, coupled by only two matrix elements; the transitional  $E2$  matrix element between them, and the diagonal  $E2$  matrix element of the  $2_1^+$  state. The GOSIA2 code performs the minimization of the  $\chi^2$  functions for the target and projectile, sharing the normalization factors as parameters across both functions, as described in detail in Ref. [59]. The normalization constants are constrained by the measured  $\gamma$ -ray intensities of the target de-excitation combined with the literature values of relevant matrix elements in the target nucleus. The vicinity of the minimum in the total  $\chi^2$  surface, defined as the sum of the  $\chi^2$  functions for both reaction partners, was then investigated as a function of the two matrix elements in the projectile nucleus:  $\langle 2_1^+ \| E2 \| 0_1^+ \rangle$  and  $\langle 2_1^+ \| E2 \| 2_1^+ \rangle$ . The minimum in the total  $\chi^2$  surface ( $\chi_{\text{min}}^2$ ) corresponds to the optimum values of these two matrix elements, while their  $1\sigma$  uncertainties can be determined by requesting that

TABLE III. Yields of observed  $\gamma$ -ray transitions in  $^{76}\text{Zn}$  and target nuclei (without correction for  $\gamma$ -ray detection efficiency), following Coulomb excitation on  $^{196}\text{Pt}$  and  $^{208}\text{Pb}$  targets, as a function of center-of-mass scattering angle. The intensities measured for  $^{196}\text{Pt}$  result from excitation of this nucleus by  $^{76}\text{Zn}$  and  $^{76}\text{Ga}$ ; in the analysis, they were corrected for the  $^{76}\text{Zn}$  beam purity equal to 70(5)%. Beam energies are expressed in MeV/nucleon.

$E_{\text{beam}}$ Target	$\theta_{\text{c.m.}}$	Nucleus	Transition	Counts	Label
2.85 $^{196}\text{Pt}$	29.0°–44.6°	$^{76}\text{Zn}$	$2_1^+ \rightarrow 0_1^+$	40 (8)	A
		$^{196}\text{Pt}$	$2_1^+ \rightarrow 0_1^+$	270 (30)	
	44.6°–59.3°	$^{76}\text{Zn}$	$2_1^+ \rightarrow 0_1^+$	55 (10)	B
		$^{196}\text{Pt}$	$2_1^+ \rightarrow 0_1^+$	290 (40)	
	59.3°–79.9°	$^{76}\text{Zn}$	$2_1^+ \rightarrow 0_1^+$	81 (16)	C
		$^{196}\text{Pt}$	$2_1^+ \rightarrow 0_1^+$	390 (50)	
	79.9°–114.8°	$^{76}\text{Zn}$	$2_1^+ \rightarrow 0_1^+$	55 (10)	D
		$^{196}\text{Pt}$	$2_1^+ \rightarrow 0_1^+$	313 (25)	
	114.8°–138.0°	$^{76}\text{Zn}$	$2_1^+ \rightarrow 0_1^+$	33 (6)	E
		$^{196}\text{Pt}$	$2_1^+ \rightarrow 0_1^+$	185 (20)	
4.0 $^{208}\text{Pb}$	28.5°–108.1°	$^{76}\text{Zn}$	$2_1^+ \rightarrow 0_1^+$	1050 (60)	
			$4_1^+ \rightarrow 2_1^+$	44 (8)	

$\chi^2 < \chi_{\text{min}}^2 + 1$  and projecting the resulting  $1\sigma$  contour on the respective axes.

The values of  $\langle 2_1^+ \| E2 \| 0_1^+ \rangle$  and  $\langle 2_1^+ \| E2 \| 2_1^+ \rangle$  obtained in the first step represent just an approximation, as the influence of multistep excitations of higher-lying states was not included in the analysis. Hence, in the second step the standard GOSIA code was used to analyze the data collected on both targets in order to determine the  $\langle 4_1^+ \| E2 \| 2_1^+ \rangle$  matrix element. All data sets listed in Tables II and III were included in the analysis for  $^{74}\text{Zn}$  and  $^{76}\text{Zn}$ , respectively. Relative normalization factors, determined from the analysis of target excitation, were introduced to link the subsets measured on  $^{196}\text{Pt}$  at 2.85 MeV/nucleon in order to preserve the sensitivity of those data to the  $\langle 2_1^+ \| E2 \| 2_1^+ \rangle$  matrix element. The  $\langle 2_1^+ \| E2 \| 0_1^+ \rangle$  value determined in the first step of the analysis, together with its uncertainty, served for absolute normalization of the measured  $\gamma$ -ray intensities, i.e., their conversion to absolute cross sections. No other spectroscopic information, in particular lifetimes of excited states, were included in the fit.

The population of the  $4_1^+$  state in Coulomb excitation depends primarily on the magnitude of the  $\langle 4_1^+ \| E2 \| 2_1^+ \rangle$  matrix element, but in the present experimental conditions the influence of the quadrupole moment of the  $4_1^+$  state on the measured excitation cross section was not negligible. For  $^{74}\text{Zn}$ , in this step of the analysis it was possible to subdivide the data collected at 4.0 MeV/nucleon into three angular ranges and estimate the  $\langle 4_1^+ \| E2 \| 4_1^+ \rangle$  matrix element from the observed angular dependence of the  $4_1^+$  excitation cross section. Figure 7 presents the distribution of  $\chi^2$  values calculated for  $^{74}\text{Zn}$  as a function of the  $\langle 4_1^+ \| E2 \| 2_1^+ \rangle$  and  $\langle 4_1^+ \| E2 \| 4_1^+ \rangle$  matrix elements. Such analysis was not possible for  $^{76}\text{Zn}$

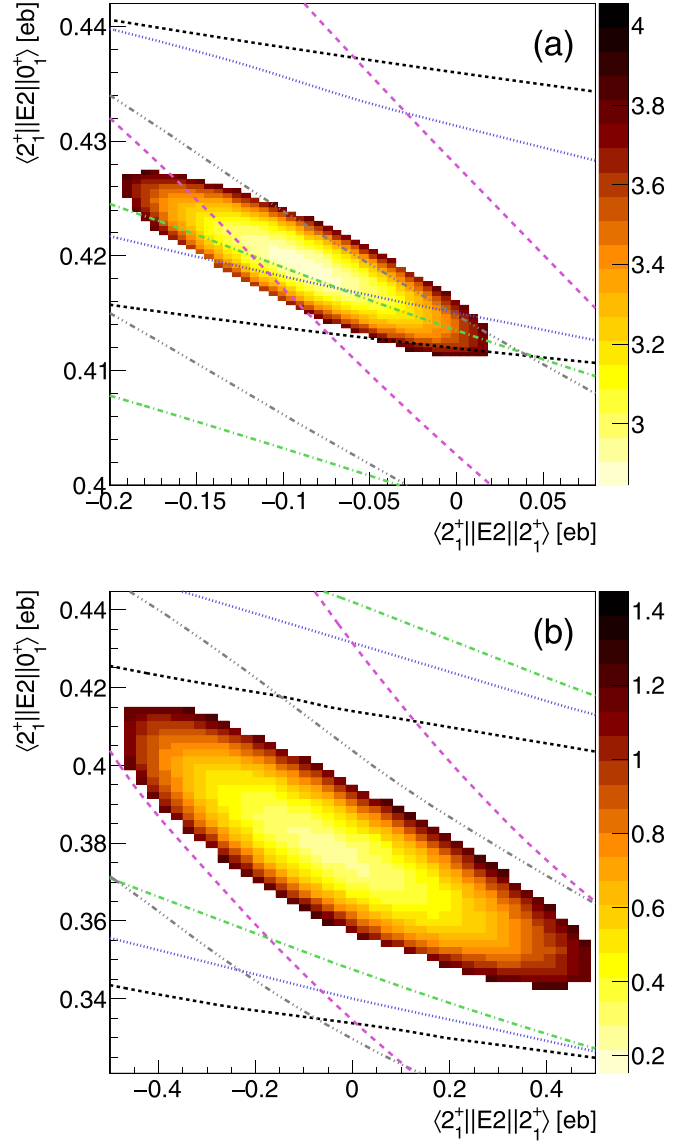


FIG. 6. Two-dimensional  $\chi^2$  surfaces with respect to the  $\langle 2_1^+ \| E2 \| 0_1^+ \rangle$  and  $\langle 2_1^+ \| E2 \| 2_1^+ \rangle$  matrix elements, for (a)  $^{74}\text{Zn}$  and (b)  $^{76}\text{Zn}$ , obtained in the final step of the analysis as explained in the text. A  $1\sigma$  cut is applied with the condition that  $\chi^2 < \chi_{\text{min}}^2 + 1$ . The data are normalized to the excitation of a 2.0-mg/cm $^2$   $^{196}\text{Pt}$  target at a beam energy of 2.85 MeV/nucleon. The lines represent individual  $1\sigma$  limits for each data set used for this analysis, listed in Tables II and III: A—black dashed, B—blue dotted, C—green dotted-dashed, D—gray dotted-dashed, and E—magenta dashed.

due to limited statistics. Consequently, it was assumed that the absolute value of the diagonal matrix element for the  $4_1^+$  state does not exceed the rotational limit calculated from the  $\langle 4_1^+ \| E2 \| 2_1^+ \rangle$  matrix element resulting from the present fit, with both negative and positive signs being considered:  $|\langle 4_1^+ \| E2 \| 4_1^+ \rangle| < 0.52$  eb.

In the third step, the GOSIA2 analysis has been repeated, but this time the level schemes for  $^{74,76}\text{Zn}$  included the  $4_1^+$  state. The  $\langle 4_1^+ \| E2 \| 2_1^+ \rangle$  and  $\langle 4_1^+ \| E2 \| 4_1^+ \rangle$  matrix elements were fixed in the analysis at the values determined in the previous



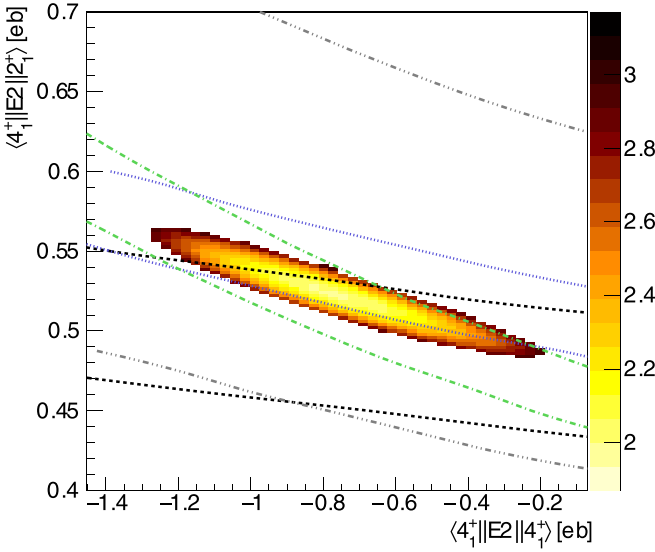


FIG. 7. Two-dimensional  $\chi^2$  surface for  $^{74}\text{Zn}$  with respect to the  $\langle 4_1^+ || E2 || 2_1^+ \rangle$  and  $\langle 4_1^+ || E2 || 4_1^+ \rangle$  matrix elements. A  $1\sigma$  cut is applied with the condition that  $\chi^2 < \chi_{\min}^2 + 1$ . For this analysis, data collected with 4.0-MeV/nucleon  $^{74}\text{Zn}$  beam on  $^{208}\text{Pb}$  and  $^{196}\text{Pt}$  targets was used. The lines represent individual  $1\sigma$  limits for each data set, see Table II: A'—black dashed, B'—blue dotted, C'—green dotted-dashed, and D'—gray dotted-dashed lines.

step. This modifies the topology of the multidimensional  $\chi^2$  surface, and consequently the values of the  $\langle 2_1^+ || E2 || 0_1^+ \rangle$  and  $\langle 2_1^+ || E2 || 2_1^+ \rangle$  matrix elements, obtained from the  $1\sigma$  cut as explained earlier, were slightly shifted. Since they influence the extracted values of the  $\langle 4_1^+ || E2 || 2_1^+ \rangle$  and  $\langle 4_1^+ || E2 || 4_1^+ \rangle$  matrix elements, steps 2 and 3 were iterated until a converged solution was obtained. Figures 6(a) and 6(b) present the total  $\chi^2$  distribution as a function of the  $\langle 2_1^+ || E2 || 0_1^+ \rangle$  and  $\langle 2_1^+ || E2 || 2_1^+ \rangle$  matrix elements, after the convergence has been reached, for  $^{74}\text{Zn}$  and  $^{76}\text{Zn}$ , respectively, Coulomb excited on a  $^{196}\text{Pt}$  target at 2.85 MeV/nucleon.

The applied procedure ensures that the final uncertainties of the fitted matrix elements include the statistical uncertainties of the  $\gamma$ -ray intensities measured for the projectile and the target, uncertainties of the literature values of the matrix elements used to describe the target excitation, as well as the correlations between all matrix elements.

The contribution to the uncertainties of the  $E2$  matrix elements, related to the uncertainty of the beam energy, was

TABLE IV. Reduced transitional and diagonal  $E2$  matrix elements in  $^{74,76}\text{Zn}$  obtained from the combined GOSIA-GOSIA2 analysis. The uncertainties are statistical only.

$E2$ matrix element	Value [eb]	
	$^{74}\text{Zn}$	$^{76}\text{Zn}$
$\langle 2_1^+    E2    0_1^+ \rangle$	0.419 (10)	0.378 (36)
$\langle 2_1^+    E2    2_1^+ \rangle$	$-0.09^{+0.12}_{-0.11}$	
$\langle 4_1^+    E2    2_1^+ \rangle$	0.52 (4)	0.55 (6)

TABLE V. Transition probabilities  $B(E2; J \rightarrow J - 2)$  and spectroscopic quadrupole moments  $Q_s$  in  $^{74,76}\text{Zn}$  determined in the present analysis, compared with the results of the previous low-energy Coulomb-excitation experiment [26] and those determined from lifetime [40,41] and intermediate-energy Coulomb-excitation [38] studies. The results of conventional large-scale shell model calculations with LNPS and JUN45 interactions, as well as Monte Carlo shell model (MCSM) predictions using A3DA-m Hamiltonian are also presented.

		$B(E2; J \rightarrow J - 2) [e^2\text{fm}^4]$					
		Present	Previous		Theory		
		$J^\pi$	Ref. [26]	Other	LNPS	MCSM	JUN45
$^{74}\text{Zn}$	$2_1^+$	351 (24)	401 (32)	$352^{+50}_{-39}$ [41] 370 (33) [40] 408 (30) [38]	390	362	309
	$4_1^+$	304 (52)	507 (74)	$116^{+32}_{-10}$ [41]	527	416	314
	$2_1^+$	285 (56)	290 (36)		340	318	276
$^{76}\text{Zn}$	$4_1^+$	330 (70)	320 (91)		457	348	270
		$J^\pi$	$Q_s [efm^2]$				
		Present					
			LNPS	MCSM	JUN45		
$^{74}\text{Zn}$	$2_1^+$	-7 (9)	-36	-22	-13		

also evaluated. The data analysis was repeated assuming that the beam energy increased by 0.7% (which corresponds to  $1\sigma$  uncertainty [51]) and then decreased by 0.7%, and the resulting matrix elements were compared. Those obtained from the GOSIA2 analysis of  $^{74,76}\text{Zn}$  on  $^{196}\text{Pt}$  at a beam energy of 2.85 MeV/nucleon changed only by 1%. A slightly larger effect of 2% was observed for the  $\langle 4_1^+ || E2 || 2_1^+ \rangle$  matrix element, determined from the analysis of data collected at 4.0 MeV/nucleon using the standard GOSIA code. These uncertainties were included in the statistical errors of the matrix elements listed in Table IV. One should note that this analysis has been done on top of the standard procedure of accounting for energy loss in the target, introduced earlier in this section.

The possible influence of higher-lying states was also investigated. Including the  $6_1^+$  state in the calculations, with the  $\langle 6_1^+ || E2 || 4_1^+ \rangle$  matrix element assumed to be equal to  $\langle 4_1^+ || E2 || 2_1^+ \rangle$ , had a negligible effect on the extracted matrix elements. The measured Coulomb-excitation cross sections in  $^{74,76}\text{Zn}$  could also be affected by the excitation of the  $2_2^+$  levels. In  $^{74}\text{Zn}$  this state has been identified at 1670 keV and its decay was observed to proceed predominantly by a 1064-keV transition to the  $2_1^+$  state [63,64]. No transition at this energy is visible in the present  $\gamma$ -ray spectra, see Fig. 3(a). An upper limit of 156 counts, corresponding to the 95% confidence level, was obtained for the  $2_2^+ \rightarrow 2_1^+$  transition using the approach proposed in Ref. [65]. This information was included in the GOSIA analysis together with the known branching ratio for the transitions de-exciting the  $2_2^+$  state. The fit yielded the upper limit for the  $B(E2; 2_2^+ \rightarrow 2_1^+)$  transition

probability equal to  $265\text{ e}^2\text{fm}^4$  (assuming negative sign of the  $\langle 0_1^+ \| E2 \| 2_1^+ \rangle \langle 2_1^+ \| E2 \| 2_2^+ \rangle \langle 2_2^+ \| E2 \| 0_1^+ \rangle$  interference term) and  $410\text{ e}^2\text{fm}^4$  for positive interference. All other matrix elements remained unchanged. A similar analysis has not been performed for  $^{76}\text{Zn}$  since no states lying close in excitation energy to the  $4_1^+$  state are known in this nucleus. However, due to important similarities of the structure of  $^{74,76}\text{Zn}$  and identical experimental conditions, it seems reasonable to assume that the impact of potential higher-lying states on the measured cross sections in  $^{76}\text{Zn}$  would also be negligible.

Figures 6(b) and 7 demonstrate that while the sensitivity of the present data to the quadrupole moments of the  $2_1^+$  state in  $^{76}\text{Zn}$  and the  $4_1^+$  state in  $^{74}\text{Zn}$  was weak, the correlation of these observables with transitional matrix elements is non-negligible and the adopted analysis method accounts for it. In fact, this correlation has a dominant contribution to the uncertainty of the  $B(E2; 4_1^+ \rightarrow 2_1^+)$  transition probabilities. Hence, even though the numbers of counts in the  $4_1^+ \rightarrow 2_1^+$  transition obtained for  $^{74}\text{Zn}$  and  $^{76}\text{Zn}$  differed by over one order of magnitude, the precision of resulting  $B(E2)$  values is comparable.

The values of transitional and diagonal  $E2$  matrix elements in  $^{74,76}\text{Zn}$  obtained from the combined GOSIA-GOSIA2 analysis are presented in Table IV. The uncertainties include all statistical contributions, including those from the uncertainties on the beam energies. However, the approximations used in the GOSIA code, in particular the semiclassical treatment of the Coulomb-excitation process, may amount to 5% of the calculated  $\gamma$ -ray intensity [59]. To account for this, the uncertainties of the  $B(E2)$  values and quadrupole moments discussed in the following section include a systematic uncertainty of 5% added in quadrature to the statistical uncertainty calculated from the values listed in Table IV.

## V. RESULTS AND DISCUSSION

The  $B(E2)$  transition probabilities and spectroscopic quadrupole moments in  $^{74,76}\text{Zn}$ , obtained in the present work, are presented in Table V, together with the results of earlier measurements as well as the predictions of three different shell-model calculations introduced in Sec. V A.

The  $B(E2; 2_1^+ \rightarrow 0_1^+)$  values in  $^{74,76}\text{Zn}$  and the  $B(E2; 4_1^+ \rightarrow 2_1^+)$  transition probability in  $^{76}\text{Zn}$ , determined in the present work, are in excellent agreement with those obtained in the previous low-energy Coulomb-excitation experiment on  $^{74,76}\text{Zn}$  [26]. The observed substantial discrepancy between the  $B(E2; 4_1^+ \rightarrow 2_1^+)$  values in  $^{74}\text{Zn}$  obtained in both Coulomb-excitation experiments and that resulting from the lifetime measurement [41] needs to be discussed in a broader context. The available data on  $B(E2; 2_1^+ \rightarrow 0_1^+)$  and  $B(E2; 4_1^+ \rightarrow 2_1^+)$  transition probabilities in  $^{62-80}\text{Zn}$  are presented in Figs. 8(a) and 8(b), respectively. Those for most stable Zn nuclei are well known from many independent lifetime and Coulomb-excitation results that yielded consistent results, and thus the evaluated values [25] are given for  $^{62,64,66,68}\text{Zn}$ . Starting from the heaviest stable Zn isotope ( $^{70}\text{Zn}$ ,  $N = 40$ ), discrepancies between the  $B(E2; 4_1^+ \rightarrow 2_1^+)$  values are present, as shown in Fig. 8(b).

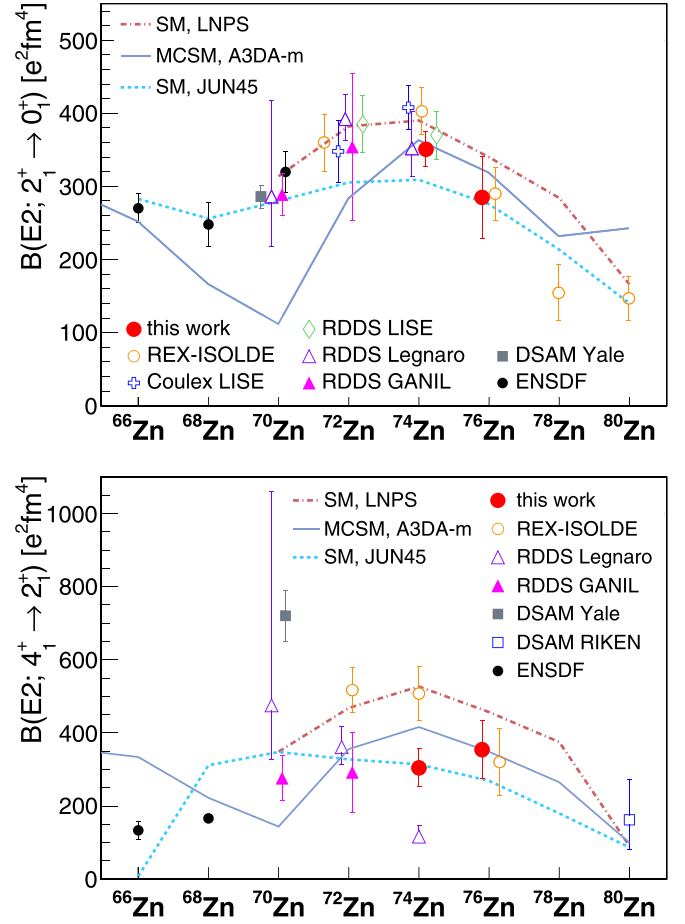


FIG. 8. Transition probabilities in even-even Zn isotopes from  $^{66}\text{Zn}$  ( $N = 36$ ) to  $^{80}\text{Zn}$  ( $N = 50$ ): a)  $B(E2; 2_1^+ \rightarrow 0_1^+)$  values, b)  $B(E2; 4_1^+ \rightarrow 2_1^+)$  values. For  $^{66,68}\text{Zn}$  only evaluated values are presented [25], while for heavier Zn isotopes the experimental results are plotted individually (REX-ISOLDE [26,30,44], Coulex LISE [37,38], RDDS LISE [40], RDDS Legnaro [41], RDDS GANIL [42], DSAM Yale [39], DSAM RIKEN [27]). Some of the points are slightly offset on the  $x$  axis for clarity. The experimental results are compared to the predictions of the large-scale shell model with the LNPS interaction (red dotted-dashed line), Monte Carlo shell model with the A3DA-m Hamiltonian (gray solid line) and large-scale shell model with the JUN45 interaction (blue dotted line).

The literature  $B(E2)$  values in even-even  $^{70-80}\text{Zn}$  isotopes result from either measurements of low-energy and intermediate-energy Coulomb-excitation cross sections, or from lifetime measurements using various reactions to populate the nuclei of interest. Intermediate-energy Coulomb-excitation measurements carried out with the LISE spectrometer at GANIL provided  $B(E2; 2_1^+ \rightarrow 0_1^+)$  values in  $^{72}\text{Zn}$  [37] and  $^{74}\text{Zn}$  [38] [blue crosses, “Coulex LISE” in Fig. 8(a)]. A series of low-energy Coulomb-excitation measurements performed at REX-ISOLDE at beam energies of about 2.8 MeV/nucleon [26,30,44] yielded  $B(E2; 2_1^+ \rightarrow 0_1^+)$  values in  $^{72,74,76,78,80}\text{Zn}$  determined relative to the observed target excitation, as well as  $B(E2; 4_1^+ \rightarrow 2_1^+)$  values in  $^{72,74,76}\text{Zn}$  [orange open circles, “REX-ISOLDE” in Figs. 8

a) and 8 b)]. The direct lifetime measurements used nonsafe Coulomb excitation to populate excited states in  $^{70}\text{Zn}$  [39,66] [filled gray squares, “DSAM Yale” in Figs. 8(a) and 8(b)], inelastic scattering and neutron knock-out at intermediate energies for states in  $^{72,74}\text{Zn}$  [40] [open green diamonds, “RDDS LISE” in Fig. 8(a)], proton knock-out at intermediate energies for states in  $^{80}\text{Zn}$  [27] [open blue square, “DSAM RIKEN” in Fig. 8(b)] and multinucleon transfer for states in  $^{70,72,74}\text{Zn}$  [open purple triangles, “RDDS Legnaro” [41] and filled magenta triangles, “RDDS GANIL” [42] in Figs. 8(a) and 8(b)].

The  $B(E2; 2_1^+ \rightarrow 0_1^+)$  values in  $^{70,72,74}\text{Zn}$  resulting from all previous measurements are in very good agreement, while a striking  $3\sigma$  disagreement (difference of a factor of four) is found between the  $B(E2; 4_1^+ \rightarrow 2_1^+)$  values in  $^{74}\text{Zn}$  obtained from low-energy Coulomb excitation [26,30] and a lifetime measurement following multinucleon transfer [41]. A  $2.7\sigma$  disagreement (difference of a factor of three) is also observed between the lifetimes of the  $4_1^+$  state in  $^{70}\text{Zn}$  resulting from measurements using multinucleon transfer [42] and nonsafe Coulomb excitation [39] to populate the state of interest. In general, all lifetimes measured in Ref. [42] ( $2_1^+$ ,  $4_1^+$  in  $^{70,72}\text{Zn}$ ,  $6_1^+$  in  $^{72}\text{Zn}$ ) are in very good agreement with those determined in Ref. [41], although in most cases the uncertainties are larger. One should also mention that preliminary results of the follow-up measurement of the  $4_1^+$  lifetimes in  $^{70,72,74}\text{Zn}$  [43], performed under similar experimental conditions, are consistent with the results of Ref. [42] for  $^{70,72}\text{Zn}$  and with that of Ref. [41] for  $^{74}\text{Zn}$ .

The origin of the observed discrepancies was investigated, but without firm conclusions. The statistics collected in the low-energy Coulomb-excitation experiments on  $^{74,76}\text{Zn}$  [26,30] were insufficient to study the evolution of excitation cross sections as a function of scattering angle, and consequently the transition probabilities were extracted under the assumption that the spectroscopic quadrupole moments of excited states were equal to zero. The same measured integral excitation cross section could be explained by a lower  $B(E2; 4_1^+ \rightarrow 2_1^+)$  value combined with large positive quadrupole moments. However, the present measurement does not provide evidence for positive quadrupole moments, and in particular that found for the  $2_1^+$  state is consistent with zero, in agreement with the assumptions used in Refs. [26,30]. Moreover, the  $B(E2; 4_1^+ \rightarrow 2_1^+)$  value in  $^{72}\text{Zn}$  obtained from a high-statistics Coulomb-excitation experiment [44] also disagrees with those resulting from lifetime measurements [41,42], although the disagreement is smaller than for  $^{74}\text{Zn}$ . The study of Ref. [44] was also capable of determining quadrupole moments of the  $2_1^+$  and  $4_1^+$  states in this nucleus, which are moderately sized and negative. This leads to a conclusion that the discrepancy observed for the  $B(E2; 4_1^+ \rightarrow 2_1^+)$  values in  $^{72,74}\text{Zn}$  cannot be attributed to the incorrect treatment of quadrupole moments in the Coulomb-excitation analysis.

The influence of possible side feeding on the determined lifetimes was also examined, in particular in Ref. [41], where the effect of introducing conditions on total excitation energy of reaction products was analyzed. Even if the lifetime analysis was limited only to events corresponding to low excitation energy, the extracted lifetime of the  $4_1^+$  state in  $^{72}\text{Zn}$  remained unchanged. Unfortunately, due to lower statistics such analy-

sis could not be performed on the data for  $^{74}\text{Zn}$ . One should note here that a recent  $\beta$ -decay study of  $^{76}\text{Zn}$  [67] found evidence for a new 25-ns high-spin isomer at 2.6 MeV. If a similar structure exists in  $^{74}\text{Zn}$ , it could be at the origin of a slow feeding of the  $4_1^+$  state, and the observed discrepancy. The recent  $\beta$ -decay studies into  $^{74}\text{Zn}$  [29,68] did not find evidence for such an isomer. This is, however, not conclusive, as the population of high-spin states in  $^{74}\text{Zn}$  via  $\beta$  decay is strongly hindered due to a low ground-state spin of the  $^{74}\text{Cu}$  mother nucleus.

### A. Shell-model calculations

To interpret the present experimental results, we performed deformed shell-model calculations for the energy spectra and  $E2$  matrix elements in  $^{74}\text{Zn}$  and  $^{76}\text{Zn}$ . These results were complemented by additional deformed Hartree-Fock and beyond-mean-field calculations within the shell-model basis. The large-scale shell-model calculations were performed using the LNPS [9] and JUN45 [1] effective interactions. The valence space of LNPS incorporates, at the  $N = 40$  interface, the degrees of freedom necessary for the description of collectivity and the breaking of the  $Z = 28$  and  $N = 40$  cores. It is composed of the  $pf$  shell for protons and the  $2p_{3/2}1f_{5/2}2p_{1/2}1g_{9/2}2d_{5/2}$  orbitals for neutrons. The present version of LNPS includes recent minor adjustments that extend its reliability up to  $N = 50$  and account for particle-hole excitations (with minor consequences at  $N = 40$ ); the effective charges are  $e_\pi = 1.31e$  and  $e_\nu = 0.46e$ . The valence space for JUN45 is restricted to the  $2p_{3/2}1f_{5/2}2p_{1/2}1g_{9/2}$  orbitals and we used the effective charges  $e_\pi = 1.8e$  and  $e_\nu = 0.8e$  recently deduced from a systematic analysis in this mass region [69]. We report in Table V the  $B(E2)$  values calculated using the LNPS and JUN45 interactions for  $^{74}\text{Zn}$  and  $^{76}\text{Zn}$ , together with those obtained with the Monte Carlo shell model (MCSM) [70,71] using the A3DA-m effective interaction [5] with effective charges  $e_\pi = 1.5e$  and  $e_\nu = 0.5e$ . The results for the spectroscopic quadrupole moment of the  $2_1^+$  state in  $^{74}\text{Zn}$  are also listed in Table V. As level energies are not the main focus of the present work, we do not present a detailed comparison with the experimental values, but note here that they are very well reproduced by all three calculations.

The systematics of the transition probabilities in the Zn isotopic chain are reported in Fig. 8. All calculations predict a parabolic behavior of the  $B(E2; 2_1^+ \rightarrow 0_1^+)$  values in  $^{70-78}\text{Zn}$  with a maximum around midshell, which is well supported by the experimental data. The consistence of the three model predictions for  $^{74,76,78}\text{Zn}$  is striking. However, in contrast with the results obtained with the LNPS and JUN45 interactions, a strong reduction of the  $B(E2; 2_1^+ \rightarrow 0_1^+)$  value is predicted by MCSM at  $N = 40$ , at variance with the experimental transition probabilities. A similar discrepancy between the MCSM predictions and those obtained with the LNPS and JUN45 interactions appears at  $N = 50$ : while the former gives almost no difference between the  $B(E2; 2_1^+ \rightarrow 0_1^+)$  values for  $^{78}\text{Zn}$  and  $^{80}\text{Zn}$ , both LNPS and JUN45 predict a decrease at  $N = 50$ , which is more pronounced for the latter. In this context, an independent measurement of the  $B(E2; 2_1^+ \rightarrow 0_1^+)$  values in  $^{78,80}\text{Zn}$  would be of much interest.

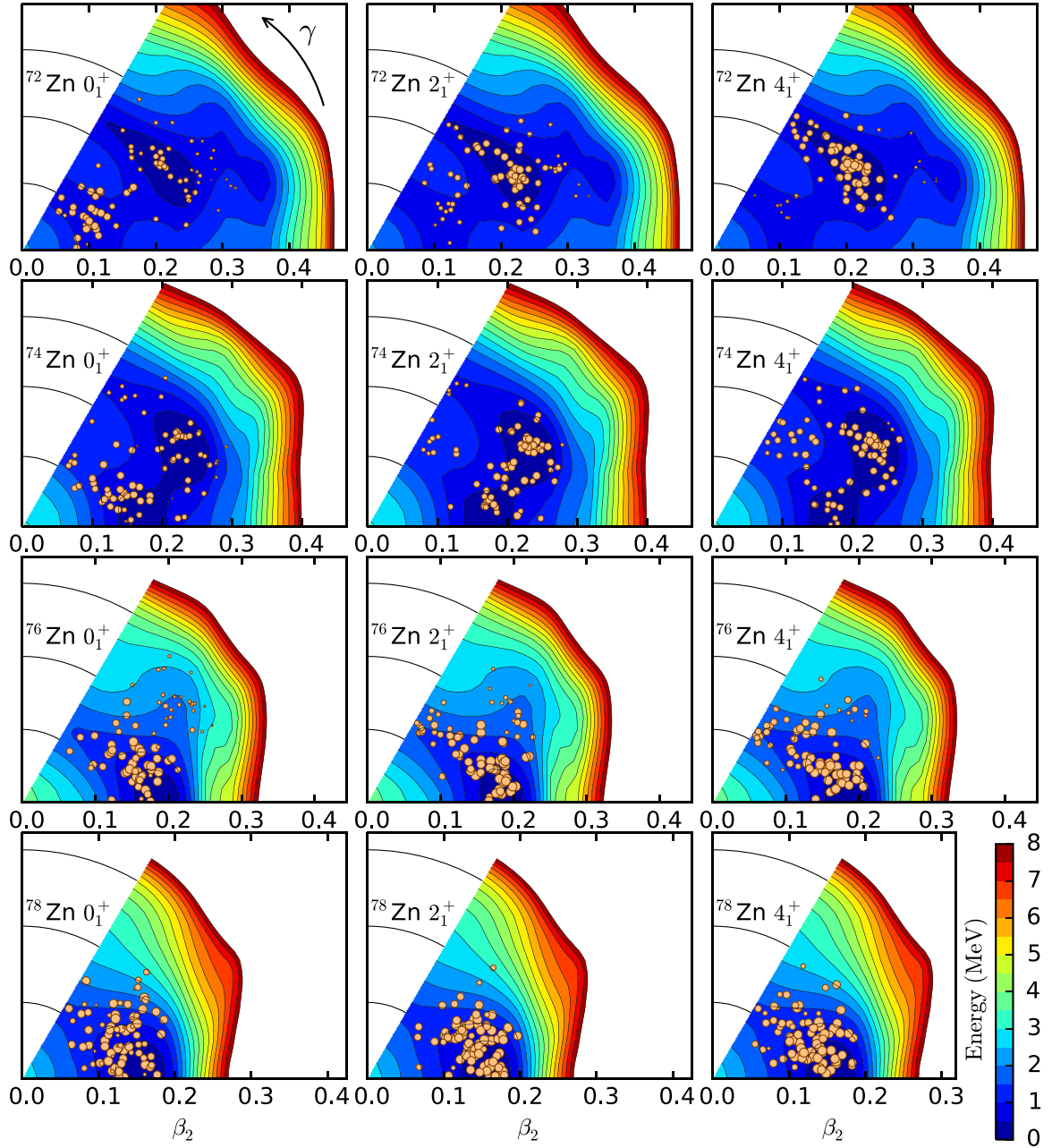


FIG. 9. T plots for the yrast states of  $^{72,74,76,78}\text{Zn}$  presenting the results of the MCSM calculations with the A3DA-m Hamiltonian. The distribution of the MCSM basis states is presented with the circles, whose sizes illustrate the importance of specific basis states in the total wave function. The circular lines of constant  $\beta_2$  deformation correspond to  $\beta_2$  values given on the  $x$  axis.

Similar to the trend observed for the  $B(E2; 2_1^+ \rightarrow 0_1^+)$  values, the calculations using the LNPS interaction predict the  $B(E2; 4_1^+ \rightarrow 2_1^+)$  values to peak at midshell and then monotonically decrease towards  $N = 50$ . MCSM calculations follow in this case a similar behavior, but again an effect of the  $N = 40$  subshell closure is visible. In contrast, calculations using the JUN45 interaction predict the  $B(E2; 4_1^+ \rightarrow 2_1^+)$  values to have a maximum at  $N = 40$  and then gradually decrease towards  $N = 50$ , with no peak at midshell. The differences between the model predictions are larger for the  $B(E2; 4_1^+ \rightarrow 2_1^+)$  values than for the  $B(E2; 2_1^+ \rightarrow 0_1^+)$  ones,

but unfortunately the existing discrepancies between the experimental results prevent concluding if any of the model descriptions provide a significantly better description of the data.

The observed parabolic behavior of the  $B(E2; 2_1^+ \rightarrow 0_1^+)$  values with a maximum around midshell observed in Fig. 8 is typical for collective nuclei. The same dependence would be expected for the seniority scheme, and the flatness of  $2_1^+$  level energies for  $^{72,74,76,78}\text{Zn}$ , evident from Fig. 1, is consistent with this picture. In this scheme, however, an inverse parabolic trend would be expected for the  $B(E2; 4_1^+ \rightarrow 2_1^+)$  values,



which correspond to seniority-conserving transitions [72]. In contrast, the  $B(E2; 4_1^+ \rightarrow 2_1^+)$  values remain rather constant with  $A$  up to  $^{74}\text{Zn}$  and although there is an increase in  $^{76}\text{Zn}$ , the value measured for  $^{80}\text{Zn}$  [27] does not confirm the trend expected for the seniority scheme.

We will now discuss in more detail the degree and type of deformation that develops in the Zn isotopes by analyzing the potential energy surfaces (PES) obtained with the A3DA-m and LNPS interactions. In Ref. [73], the T plots [5] presenting MCSM basis vector distributions on the potential energy surfaces (PES), obtained by the constrained Hartree-Fock (CHF) calculations for the A3DA-m interaction, were shown for the  $0_1^+$ ,  $2_1^+$ , and  $4_1^+$  states of  $^{72,74}\text{Zn}$ . These are displayed in the upper part of Fig. 9, together with new T plots for  $^{76,78}\text{Zn}$  shown in its bottom part. All PESs in Fig. 9 exhibit rather flat minima, extending both in the  $\beta$  and  $\gamma$  directions, related to widely diffused MCSM basis vector distributions. Such distributions imply substantial fluctuations of the wave functions on the  $\beta$ - $\gamma$  plane. While the softness in  $\gamma$  seems similar for both  $^{72,74}\text{Zn}$ , the softness in  $\beta$  is less pronounced for  $^{74}\text{Zn}$  than for  $^{72}\text{Zn}$ . Similar conclusions can be drawn from beyond-mean-field calculations using the symmetry-conserving configuration mixing (SCCM) approach and the D1S Gogny interaction [36], which suggest that the triaxial degree of freedom is important in the description of  $^{70,72,74}\text{Zn}$ . The ground states of these nuclei were predicted by SCCM to evolve from a  $\gamma$ - and  $\beta$ -soft  $^{70}\text{Zn}$  to a more prolate-deformed, but still rather soft  $^{74}\text{Zn}$ . Considerable  $\gamma$  softness was also predicted for  $^{64,66,68}\text{Zn}$  by beyond-mean-field calculations with the relativistic PC-PK1 functional [74], and for  $^{68,72}\text{Zn}$  by more recent calculations with the DD-PC1 and NL3\* functionals [75]. Very recently, the impact of the triaxial degree of freedom on the structure of  $^{66}\text{Zn}$  has been discussed on the basis of several different shell-model and SCCM calculations supported by experimental results [32].

The T plots for the  $^{72,74,76,78}\text{Zn}$  nuclei, presented in Fig. 9, show several basic features. First, none of the states shown are spherical: there are no circles close to  $\beta_2 = 0$ . This is very different from the patterns observed for the Ni isotopes, presented in Fig. 3 of Ref. [5] (to facilitate the comparison, note that  $\beta_2$  and  $\langle Q_0 \rangle$  can be related by  $\beta_2 \approx 4/3 \cdot 10^{-3} \langle Q_0 \rangle$  where  $\langle Q_0 \rangle$  is in units of  $\text{fm}^2$ ). Such deviations from sphericity contradict the assumption of the seniority scheme; indeed, as discussed above, this scheme does not hold for the Zn isotopes. Secondly, neither a prolate nor oblate shape is realized, and each state in Fig. 9 is composed of various triaxial shapes. In the Ni isotopes, the prolate local minimum, or its remnant, remains on the PES up to  $N = 48$ , but this is not the case in the Zn isotopes. In the Ni isotopes, protons are excited from the  $f_{7/2}$  orbital to higher  $pf$ -shell orbitals creating a few holes in the  $f_{7/2}$  orbital. Those holes tend to generate prolate deformation, leading to the appearance of prolate local minima, or their remnants, in the PES. This mechanism is gone in Zn isotopes because of two extra protons beyond  $Z = 28$  suppressing the excitation from the  $f_{7/2}$  proton shell, and consequently the prolate minima do not appear. Thirdly, there is no dominant shape in Fig. 9, and substantial fluctuations are found. In  $^{72,74}\text{Zn}$ , the deformation increases when going from the  $0_1^+$  ground state to the first excited  $2_1^+$  state, consistent with

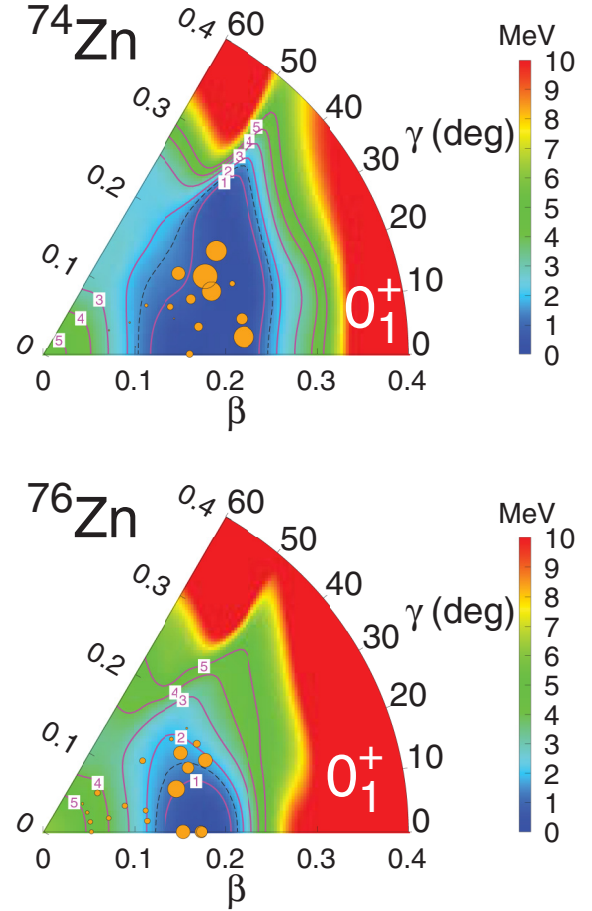


FIG. 10. Potential energy surfaces from constrained Hartree-Fock minimization in the shell-model basis for  $^{74}\text{Zn}$  (up) and  $^{76}\text{Zn}$  (bottom). Orange circles represent the amplitudes of the final ground-state wave functions in the DNO-SM basis.

the vibrational character of the latter. In contrast, for  $^{76,78}\text{Zn}$  the deformations of the  $0_1^+$ ,  $2_1^+$ , and  $4_1^+$  states are similar. In these nuclei, the PES becomes narrow, and the T-plot circles are pushed into a small bottom area. The experimental findings appear to be generally consistent with these features.

Along the same line, we have performed deformed Hartree-Fock and beyond-mean-field calculations within the LNPS shell-model basis for both  $^{74}\text{Zn}$  and  $^{76}\text{Zn}$ . In Fig. 10 we show the PES resulting from these CHF calculations. At the mean-field level, these two nuclei exhibit nonspherical minima with  $\beta$  deformation around 0.2. In  $^{76}\text{Zn}$ , the minimum develops around axial shapes whereas in  $^{74}\text{Zn}$  a much broader minimum area, extending towards triaxial shapes, is observed. The diagonalization of the Hamiltonian in the framework of the discrete nonorthogonal shell model (DNO-SM), recently developed in Ref. [76], is then obtained after rotational symmetry restoration using the angular-momentum projection technique. The expansion of the final ground-state wave functions in the  $(\beta, \gamma)$  plane is also shown in Fig. 10. Indeed, after full shell-model diagonalization, the obtained spectra and associated  $B(E2)$  values are in overall good agreement

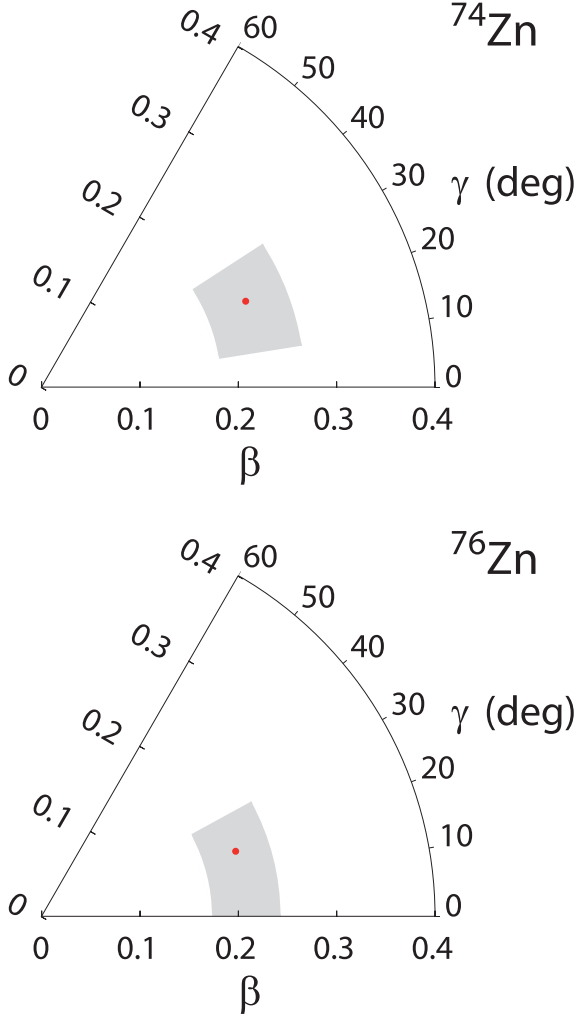


FIG. 11.  $1\sigma$  contours in the  $\beta$ - $\gamma$  sextant for the ground states of  $^{74}\text{Zn}$  (top) and  $^{76}\text{Zn}$  (bottom) obtained from the analysis of the quadrupole invariants using the LNPS effective interaction. The red dots represent the effective  $\beta$  and  $\gamma$  values.

with experimental data as shown in Table V. The  $(\beta, \gamma)$  plots obtained from the Kumar invariants [77] using the calculated  $E2$  matrix elements are provided in Fig. 11. They agree very well with the potential energy surfaces in Fig. 10, both of them pointing to fully correlated wave functions with triaxial shapes and rather large fluctuations. In general, one can observe that the results from both the DNO-SM diagonalization as well as from the standard SM diagonalization followed by the analysis of Kumar observables are fully consistent with the interpretation resulting from the MCSM calculations discussed above.

The quadrupole moment of the  $2_1^+$  state in  $^{74}\text{Zn}$  is consistent with zero. This result is presented in Fig. 12, together with the experimental values obtained for lighter Zn nuclei, and those resulting from the present shell-model calculations. It can be observed that most quadrupole-moment measurements for even-even Zn nuclei with  $A \geq 66$  yielded values considerably lower than what one would deduce from the  $B(E2; 2_1^+ \rightarrow 0_1^+)$  values assuming an axial rotor model. The same

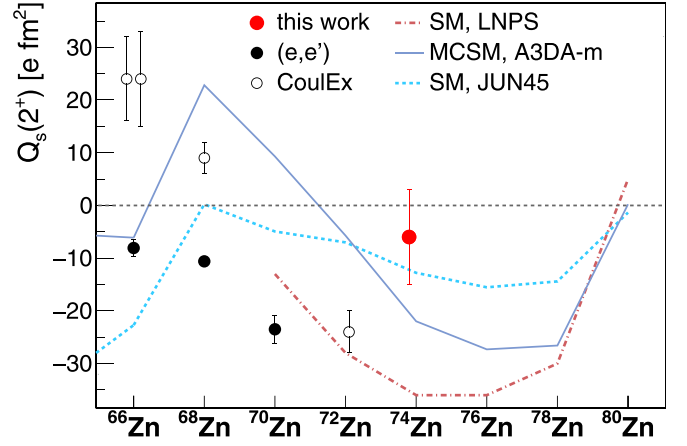


FIG. 12. Spectroscopic quadrupole moments of the  $2_1^+$  states in even-even Zn isotopes from  $^{66}\text{Zn}$  ( $N = 36$ ) to  $^{80}\text{Zn}$  ( $N = 50$ ). The result of the present measurement, plotted with a red filled circle, is compared to the literature values from electron scattering ([78], black filled circles) and Coulomb excitation ([32–34,44], black open circles) as well as the predictions of the large-scale shell model with the LNPS interaction (red dotted-dashed line), Monte Carlo shell model with the A3DA-m Hamiltonian (gray solid line) and large-scale shell model with the JUN45 interaction (blue dotted line).

is true for the values resulting from the calculations with the JUN45 interaction. This is consistent with an important role of triaxiality in the Zn isotopic chain, observed in the above-mentioned theoretical and experimental studies. The MCSM calculations seem to predict an evolution from weak axial oblate deformation for  $^{68}\text{Zn}$  [positive value of  $Q_s(2_1^+)$ ], via  $\gamma$ -soft shapes for  $^{70,72}\text{Zn}$  [ $Q_s(2_1^+)$  very close to zero], towards axially symmetric weakly prolate-deformed ones close to  $N = 50$  [ $Q_s(2_1^+)$  negative and close to the rotational estimate]. This trend of static quadrupole moments is consistent with the T plots shown in Fig. 9. For  $^{74}\text{Zn}$ , the present spectroscopic quadrupole moment for the  $2_1^+$  state and the  $B(E2; 4_1^+ \rightarrow 2_1^+)$  value are overestimated by both the MCSM and LSSM calculations with the LNPS interaction. This could be eventually related to the extended flat PES minimum area, where in particular  $K$  mixing could quench these two quantities, even though the exact mechanism is difficult to trace back.

It is important to note here that for a  $\gamma$ -soft nucleus it is expected that the centroid of the wave-function distribution will correspond to  $\langle \gamma \rangle = 30^\circ$  and the quadrupole moments of excited states will be equal to zero. However, in the vicinity of  $\gamma = 30^\circ$ , small variations of this parameter translate into large changes of the spectroscopic quadrupole moments, both in terms of sign and magnitude. Consequently, accurate predictions of quadrupole moments for nuclei exhibiting important  $\gamma$  softness are extremely difficult, as outlined in Ref. [32].

Finally, it is worth noting that the reduction of the  $Q_s(2_1^+)$  in  $^{74}\text{Zn}$  could be also attributed to shape coexistence and mixing. Indeed, the shape-coexistence phenomenon seems to be prevalent in the vicinity of  $^{68}\text{Ni}$  and  $^{78}\text{Ni}$  [17,24,79,80] and the energies of the  $0_2^+$  states in  $^{66,68,70,72,74}\text{Zn}$  nuclei follow a parabolic trend characteristic for intruder configurations,

as discussed in Sec. II. However, the excitation energy of the  $0_2^+$  state in  $^{74}\text{Zn}$  is considerably higher than those of its counterparts in the lighter Zn isotopes. Consequently, it is more difficult to imagine that a  $2_3^+$  state built on the intruder configuration would strongly mix with the  $2_1^+$  state, leading to the reduction of the quadrupole moment of the latter. Such a scenario is also not supported by shell-model calculations of Ref. [29], which suggest instead that the ground-state band and the band built on the  $0_2^+$  state in  $^{74}\text{Zn}$  correspond to similar average deformations, but with a different degree of softness, and that the mixing between these two structures is weak. Clearly, more experimental work is needed to understand the origin of the low  $Q_s(2_1^+)$  value and  $B(E2; 4_1^+ \rightarrow 2_1^+)/B(E2; 2_1^+ \rightarrow 0_1^+)$  ratio in  $^{74}\text{Zn}$ .

## VI. SUMMARY

The first experiment using radioactive beams post-accelerated by the HIE-ISOLDE facility is reported. It has benefited from a substantial gain in cross sections for the multistep Coulomb-excitation process due to the increase of available beam energy. The obtained  $B(E2; 2_1^+ \rightarrow 0_1^+)$  transition probabilities in  $^{74,76}\text{Zn}$  are in agreement with the results of the previous low-energy Coulomb-excitation experiment to study neutron-rich Zn nuclei [26]. While the  $B(E2; 4_1^+ \rightarrow 2_1^+)$  transition probability in  $^{76}\text{Zn}$  is also in agreement with the earlier Coulomb-excitation result, the value obtained for  $^{74}\text{Zn}$  is considerably lower. The spectroscopic quadrupole moment of the  $2_1^+$  state in  $^{74}\text{Zn}$  was determined and its value is consistent with zero, which can be related to shape coexistence or triaxiality. The shell-model calculations performed in various valence spaces show a very good agreement with the measured  $B(E2; 2_1^+ \rightarrow 0_1^+)$  values for  $^{74,76}\text{Zn}$ , even though there exist minor discrepancies between the transition probabilities in the isotopic Zn chain predicted within the three approaches.

All three calculations also agree fairly well in the predictions for the  $B(E2; 4_1^+ \rightarrow 2_1^+)$  value in  $^{76}\text{Zn}$ . The new experimental value for the  $B(E2; 4_1^+ \rightarrow 2_1^+)$  transition probability in  $^{74}\text{Zn}$  does not resolve the previous disagreement between the measured values. Potential energy surfaces obtained in the framework of constrained Hartree-Fock calculations put in evidence the triaxial degree of deformation in both studied Zn isotopes. Moreover, the Kumar analysis of the shell-model wave functions shows large fluctuations in the deformation parameters.

## ACKNOWLEDGMENTS

We thank the ISOLDE collaboration and technical staff for outstanding assistance during the experiment. This project has received funding from the European Union's Horizon 2020 research and innovation programme under Grant Agreement No. 654002 (ENSAR2), from Research Foundation Flanders (FWO, Belgium) under GOA/2015/010 (BOF KU Leuven), from the FWO and F.R.S.-FNRS under the Excellence of Science (EOS) programme (No. 40007501), from the German BMBF under Contract No. 05P15PKCIA and Verbundprojekt 05P2015 and under Contract No. 05P21PKCI1 and Verbundprojekt 05P2021, from the Polish Ministry of Education and Science under Contract No. 2021/WK/07, from the Spanish Grant No. PID2019-104390Gb-I00 funded by MCIN/AEI/10.13039/501100011033, from the Polish National Science Centre, Grant No. 2014/12/S/ST2/00483, from MEXT as the HPCI Strategic Program (The origin of matter and the universe) and "Program for Promoting Researches on the Supercomputer Fugaku" (simulation for basic science: from fundamental laws of particles to creation of nuclei), and from JICFuS. The MCSM calculations were performed on K computer at RIKEN AICS (Proposals No. hp120284 and No. hp130024).

- 
- [1] M. Honma, T. Otsuka, T. Mizusaki, and M. Hjorth-Jensen, *Phys. Rev. C* **80**, 064323 (2009).
  - [2] K. Sieja, F. Nowacki, K. Langanke, and G. Martínez-Pinedo, *Phys. Rev. C* **79**, 064310 (2009).
  - [3] K. Sieja and F. Nowacki, *Phys. Rev. C* **85**, 051301(R) (2012).
  - [4] T. Otsuka, T. Suzuki, M. Honma, Y. Utsuno, N. Tsunoda, K. Tsukiyama, and M. Hjorth-Jensen, *Phys. Rev. Lett.* **104**, 012501 (2010).
  - [5] Y. Tsunoda, T. Otsuka, N. Shimizu, M. Honma, and Y. Utsuno, *Phys. Rev. C* **89**, 031301(R) (2014).
  - [6] T. Otsuka, A. Gade, O. Sorlin, T. Suzuki, and Y. Utsuno, *Rev. Mod. Phys.* **92**, 015002 (2020).
  - [7] T. Otsuka and Y. Tsunoda, *J. Phys. G: Nucl. Part. Phys.* **43**, 024009 (2016).
  - [8] F. Nowacki, A. Poves, E. Caurier, and B. Bounthong, *Phys. Rev. Lett.* **117**, 272501 (2016).
  - [9] S. M. Lenzi, F. Nowacki, A. Poves, and K. Sieja, *Phys. Rev. C* **82**, 054301 (2010).
  - [10] T. Otsuka, T. Suzuki, R. Fujimoto, H. Grawe, and Y. Akaishi, *Phys. Rev. Lett.* **95**, 232502 (2005).
  - [11] S. Suchyta, S. N. Liddick, Y. Tsunoda, T. Otsuka, M. B. Bennett, A. Chemey, M. Honma, N. Larson, C. J. Prokop, S. J. Quinn, N. Shimizu, A. Simon, A. Spyrou, V. Tripathi, Y. Utsuno, and J. M. VonMoss, *Phys. Rev. C* **89**, 021301(R) (2014).
  - [12] F. Flavigny, D. Pauwels, D. Radulov, I. J. Darby, H. De Witte, J. Diriken, D. V. Fedorov, V. N. Fedosseev, L. M. Fraile, M. Huyse, V. S. Ivanov, U. Köster, B. A. Marsh, T. Otsuka, L. Popescu, R. Raabe, M. D. Seliverstov, N. Shimizu, A. M. Sjödin, Y. Tsunoda *et al.*, *Phys. Rev. C* **91**, 034310 (2015).
  - [13] C. J. Chiara, D. Weisshaar, R. V. F. Janssens, Y. Tsunoda, T. Otsuka, J. L. Harker, W. B. Walters, F. Recchia, M. Albers, M. Alcorta, V. M. Bader, T. Baugher, D. Bazin, J. S. Berryman, P. F. Bertone, C. M. Campbell, M. P. Carpenter, J. Chen, H. L. Crawford, H. M. David *et al.*, *Phys. Rev. C* **91**, 044309 (2015).
  - [14] A. Morales, G. Benzoni, H. Watanabe, Y. Tsunoda, T. Otsuka, S. Nishimura, F. Browne, R. Daido, P. Doornenbal, Y. Fang, G. Lorusso, Z. Patel, S. Rice, L. Sinclair, P.-A. Söderström, T. Sumikama, J. Wu, Z. Xu, A. Yagi, R. Yokoyama *et al.*, *Phys. Lett. B* **765**, 328 (2017).

- [15] S. Franchoo, M. Huyse, K. Kruglov, Y. Kudryavtsev, W. F. Mueller, R. Raabe, I. Reusen, P. Van Duppen, J. Van Roosbroeck, L. Vermeeren, A. Wöhr, K.-L. Kratz, B. Pfeiffer, and W. B. Walters, *Phys. Rev. Lett.* **81**, 3100 (1998).
- [16] K. T. Flanagan, P. Vingerhoets, M. Avgouleas, J. Billowes, M. L. Bissell, K. Blaum, B. Cheal, M. DeRydt, V. N. Fedosseev, D. H. Forest, C. Geppert, U. Köster, M. Kowalska, J. Krämer, K. L. Kratz, A. Krieger, E. Mané, B. A. Marsh, T. Materna, L. Mathieu *et al.*, *Phys. Rev. Lett.* **103**, 142501 (2009).
- [17] S. Leoni, B. Fornal, N. Mărginean, M. Sferrazza, Y. Tsunoda, T. Otsuka, G. Bocchi, F. C. L. Crespi, A. Bracco, S. Aydin, M. Boromiza, D. Bucurescu, N. Cieplicka-Oryńczak, C. Costache, S. Călinescu, N. Florea, D. G. Ghiță, T. Glodariu, A. Ionescu, L. W. Iskra *et al.*, *Phys. Rev. Lett.* **118**, 162502 (2017).
- [18] Y. Ichikawa, H. Nishibata, Y. Tsunoda, A. Takamine, K. Imamura, T. Fujita, T. Sato, S. Momiyama, Y. Shimizu, D. Ahn, K. Asahi, H. Baba, D. Balabanski, F. Boulay, J. Daugas, T. Egami, N. Fukuda, C. Funayama, T. Furukawa, G. Georgiev *et al.*, *Nat. Phys.* **15**, 321 (2019).
- [19] N. Mărginean, D. Little, Y. Tsunoda, S. Leoni, R. V. F. Janssens, B. Fornal, T. Otsuka, C. Michelagnoli, L. Stan, F. C. L. Crespi, C. Costache, R. Lica, M. Sferrazza, A. Turturica, A. D. Ayangeakaa, K. Auranen, M. Barani, P. C. Bender, S. Bottoni, M. Boromiza *et al.*, *Phys. Rev. Lett.* **125**, 102502 (2020).
- [20] F. Bello Garrote, E. Sahin, Y. Tsunoda, T. Otsuka, A. Gorgen, M. Niikura, S. Nishimura, G. de Angelis, G. Benzoni, A. Morales, V. Modamio, Z. Xu, H. Baba, F. Browne, A. Bruce, S. Ceruti, F. Crespi, R. Daido, M.-C. Delattre, P. Doornenbal *et al.*, *Phys. Rev. C* **102**, 034314 (2020).
- [21] E. Sahin, F. L. Bello Garrote, Y. Tsunoda, T. Otsuka, G. deAngelis, A. Gorgen, M. Niikura, S. Nishimura, Z. Y. Xu, H. Baba, F. Browne, M. C. Delattre, P. Doornenbal, S. Franchoo, G. Gey, K. Hadyńska-Klęk, T. Isobe, P. R. John, H. S. Jung, I. Kojouharov *et al.*, *Phys. Rev. Lett.* **118**, 242502 (2017).
- [22] L. Olivier, S. Franchoo, M. Niikura, Z. Vajta, D. Sohler, P. Doornenbal, A. Obertelli, Y. Tsunoda, T. Otsuka, G. Authélet, H. Baba, D. Calvet, F. Château, A. Corsi, A. Delbart, J.-M. Gheller, A. Gillibert, T. Isobe, V. Lapoux, M. Matsushita *et al.*, *Phys. Rev. Lett.* **119**, 192501 (2017).
- [23] A. Welker, N. A. S. Althubiti, D. Atanasov, K. Blaum, T. E. Cocolios, F. Herfurth, S. Kreim, D. Lunney, V. Manea, M. Mougeot, D. Neidherr, F. Nowacki, A. Poves, M. Rosenbusch, L. Schweikhard, F. Wienholtz, R. N. Wolf, and K. Zuber, *Phys. Rev. Lett.* **119**, 192502 (2017).
- [24] R. Taniuchi, C. Santamaria, P. Doornenbal, A. Obertelli, K. Yoneda, G. Authélet, H. Baba, D. Calvet, F. Château, A. Corsi, A. Delbart, J.-M. Gheller, A. Gillibert, J. Holt, T. Isobe, V. Lapoux, M. Matsushita, J. Menéndez, S. Momiyama, T. Motobayashi *et al.*, *Nature* **569**, 53 (2019).
- [25] Data extracted using the NNDC On-Line Data Service from the ENSDF database, files revised as of March 2009 ( $^{66}\text{Zn}$ ), March 2012 ( $^{68}\text{Zn}$ ), July 2016 ( $^{70}\text{Zn}$ ), May 2009 ( $^{72}\text{Zn}$ ), March 2017 ( $^{74}\text{Zn}$ ), March 1994 ( $^{76}\text{Zn}$ ), June 2009 ( $^{78}\text{Zn}$ ), August 2014 ( $^{80}\text{Zn}$ ), and June 2007 ( $^{196}\text{Pt}$ ), <http://www.nndc.bnl.gov/nndc/ensdf/>.
- [26] J. Van de Walle, F. Aksouh, T. Behrens, V. Bildstein, A. Blazhev, J. Cederkäll, E. Clément, T. Cocolios, T. Davinson, P. Delahaye, J. Eberth, A. Ekström, D. Fedorov, V. Fedosseev, L. Fraile, S. Franchoo, R. Gernhäuser, G. Georgiev, D. Habs, K. Heyde *et al.*, *Phys. Rev. C* **79**, 014309 (2009).
- [27] Y. Shiga, K. Yoneda, D. Steppenbeck, N. Aoi, P. Doornenbal, J. Lee, H. Liu, M. Matsushita, S. Takeuchi, H. Wang, H. Baba, P. Bednarczyk, Z. Dombradi, Z. Fulop, S. Go, T. Hashimoto, M. Honma, E. Ideguchi, K. Ieki, K. Kobayashi *et al.*, *Phys. Rev. C* **93**, 024320 (2016).
- [28] C. Shand, Z. Podolyák, M. Górska, P. Doornenbal, A. Obertelli, F. Nowacki, T. Otsuka, K. Sieja, J. Tostevin, Y. Tsunoda, G. Authélet, H. Baba, D. Calvet, A. Château, S. Chen, A. Corsi, A. Delbart, J. Gheller, A. Giganon, A. Gillibert *et al.*, *Phys. Lett. B* **773**, 492 (2017).
- [29] M. Rocchini, P. E. Garrett, M. Zielińska, S. M. Lenzi, D. D. Dao, F. Nowacki, V. Bildstein, A. D. MacLean, B. Olaizola, Z. T. Ahmed, C. Andreoiu, A. Babu, G. C. Ball, S. S. Bhattacharjee, H. Bidaman, C. Cheng, R. Coleman, I. Dillmann, A. B. Garnsworthy, S. Gillespie *et al.*, *Phys. Rev. Lett.* **130**, 122502 (2023).
- [30] J. Van de Walle, F. Aksouh, F. Ames, T. Behrens, V. Bildstein, A. Blazhev, J. Cederkäll, E. Clément, T. Cocolios, T. Davinson, P. Delahaye, J. Eberth, A. Ekström, D. Fedorov, V. Fedosseev, L. Fraile, S. Franchoo, R. Gernhäuser, G. Georgiev, D. Habs *et al.*, *Phys. Rev. Lett.* **99**, 142501 (2007).
- [31] L. Wilets and M. Jean, *Phys. Rev.* **102**, 788 (1956).
- [32] M. Rocchini, K. Hadyńska-Klęk, A. Nannini, A. Goasduff, M. Zielinska, D. Testov, T. R. Rodríguez, A. Gargano, F. Nowacki, G. DeGregorio, H. Naïdja, P. Sona, J. J. Valiente-Dobón, D. Mengoni, P. R. John, D. Bazzacco, G. Benzoni, A. Bosso, P. Cocconi, M. Chiari *et al.*, *Phys. Rev. C* **103**, 014311 (2021).
- [33] M. Koizumi, A. Seki, Y. Toh, M. Oshima, A. Osa, A. Kimura, Y. Hatsukawa, T. Shizuma, T. Hayakawa, M. Matsuda, J. Katakura, T. Czosnyka, M. Sugawara, T. Morikawa, and H. Kusakari, *Eur. Phys. J. A* **18**, 87 (2003).
- [34] M. Koizumi, A. Seki, Y. Toh, A. Osa, Y. Utsuno, A. Kimura, M. Oshima, T. Hayakawa, Y. Hatsukawa, J. Katakura, M. Matsuda, T. Shizuma, T. Czosnyka, M. Sugawara, T. Morikawa, and H. Kusakari, *Nucl. Phys. A* **730**, 46 (2004).
- [35] E. Fiori, G. Georgiev, A. E. Stuchbery, A. Jungclaus, D. L. Balabanski, A. Blazhev, S. Cabaret, E. Clement, M. Danchev, J. M. Daugas, S. Grevy, M. Hass, V. Kumar, J. Leske, R. Lozeva, S. Lukyanov, T. J. Mertzimekis, V. Modamio, B. Mouginot, F. Nowacki *et al.*, *Phys. Rev. C* **85**, 034334 (2012).
- [36] A. Illana, A. Jungclaus, R. Orlandi, A. Perea, C. Bauer, J. A. Briz, J. L. Egido, R. Gernhäuser, J. Leske, D. Mücher, J. Pakarinen, N. Pietralla, M. Rajabali, T. R. Rodríguez, D. Seiler, C. Stahl, D. Voulot, F. Wenander, A. Blazhev, H. DeWitte *et al.*, *Phys. Rev. C* **89**, 054316 (2014).
- [37] S. Leenhardt, O. Sorlin, M. Porquet, F. Azaiez, J. Angélique, M. Belleguic, C. Borcea, C. Bourgeois, J. Daugas, C. Donzau, I. Deloncle, J. Duprat, A. Gillibert, S. Grévy, D. Guillemaud-Mueller, J. Kiener, M. Lewitowicz, S. Lukyanov, F. Marie, N. Orr *et al.*, *Eur. Phys. J. A* **14**, 1 (2002).
- [38] O. Perru, O. Sorlin, S. Franchoo, F. Azaiez, E. Bouchez, C. Bourgeois, A. Chatillon, J. M. Daugas, Z. Dlouhy, Z. Dombradi, C. Donzau, L. Gaudefroy, H. Grawe, S. Grevy, D. Guillemaud-Mueller, F. Hammache, F. Ibrahim, Y. LeCoz, S. M. Lukyanov, I. Matea *et al.*, *Phys. Rev. Lett.* **96**, 232501 (2006).
- [39] D. Mücher, G. Gürdal, K. H. Speidel, G. J. Kumbartzki, N. Benczer-Koller, S. J. Q. Robinson, Y. Y. Sharon, L. Zamick, A. F. Lisetskiy, R. J. Casperson, A. Heinz, B. Krieger, J. Leske, P. Maier-Komor, V. Werner, E. Williams, and R. Winkler, *Phys. Rev. C* **79**, 054310 (2009).



- [40] M. Niikura, B. Mouginot, S. Franchoo, I. Matea, I. Stefan, D. Verney, F. Azaiez, M. Assie, P. Bednarczyk, C. Borcea, A. Burger, G. Burgunder, A. Buta, L. Cáceres, E. Clément, L. Coquard, G. de Angelis, G. de France, F. de Oliveira Santos, A. Dewald *et al.*, *Phys. Rev. C* **85**, 054321 (2012).
- [41] C. Louchart, A. Obertelli, A. Görgen, W. Korten, D. Bazzacco, B. Birkenbach, B. Bruyneel, E. Clément, P. Coleman-Smith, L. Corradi, D. Curien, G. de Angelis, G. de France, J.-P. Delaroche, A. Dewald, F. Didierjean, M. Doncel, G. Duchêne, J. Eberth, M. Erduran *et al.*, *Phys. Rev. C* **87**, 054302 (2013).
- [42] I. Čeliković, A. Dijon, E. Clément, G. de France, P. Van Isacker, J. Ljungvall, C. Fransen, G. Georgiev, A. Gottardo, M. Hackstein, T. Hagen, C. Louchart, P. Napiorkowski, A. Obertelli, F. Recchia, W. Rother, S. Siem, B. Sulignano, P. Ujic, J. Valiente-Dobón *et al.*, *Acta Phys. Pol. B* **44**, 375 (2013).
- [43] T. Milanović, I. Čeliković, C. Michelagnoli, G. de France, A. Boso, T. Braunroth, E. Clément, A. Dewald, G. Georgiev, E. Ideguchi, B. Jacquot, W. Królas, D. Napoli, N. Lalović, K. Lee, A. Lemasson, H. Li, J. Ljungvall, A. Navin, A. Nori *et al.*, *Acta Phys. Pol. B* **51**, 837 (2020).
- [44] S. Hellgartner, D. Mücher, K. Wimmer, V. Bildstein, J. Egido, R. Gernhäuser, R. Krücken, A. Nowak, M. Zielińska, C. Bauer, M. Benito, S. Bottoni, H. De Witte, J. Elseviers, D. Fedorov, F. Flavigny, A. Illana, M. Klintefjord, T. Kröll, R. Lutter *et al.*, *Phys. Lett. B* **841**, 137933 (2023).
- [45] V. Fedosseev, K. Chrysalidis, T. Day Goodacre, B. Marsh, S. Rothe, C. Seiffert, and K. Wendt, *J. Phys. G: Nucl. Part. Phys.* **44**, 084006 (2017).
- [46] F. Ames, G. Bollen, P. Delahaye, O. Forstner, G. Huber, O. Kester, K. Reisinger, and P. Schmidt, *Nucl. Instrum. Methods Phys. Res. A* **538**, 17 (2005).
- [47] F. Wenander, *J. Instrum.* **5**, C10004 (2010).
- [48] Y. Kadi, Y. Blumenfeld, W. Venturini Delsolaro, M. Fraser, M. Huyse, A. Papageorgiou Koufidou, J. Rodriguez, and F. Wenander, *J. Phys. G: Nucl. Part. Phys.* **44**, 084003 (2017).
- [49] M. Borge and K. Riisager, *Eur. Phys. J. A* **52**, 334 (2016).
- [50] D. Cline, *Bull. Am. Phys. Soc.* **14**, 726 (1969).
- [51] J. Rodriguez, N. Bidault, E. Bravin, R. Catherall, E. Fadakis, P. Fernier, M. Fraser, M. Garcia Borge, K. Hanke, M. Huyse, K. Johnston, Y. Kadi, M. Kowalska, M. Lozano Benito, E. E. Matli, J. Pakarinen, E. Rapisarda, S. Sadovich, E. Siesling, P. Van Duppen *et al.*, *Proceedings of the International Particle Accelerator Conference (IPAC'16), Busan, Korea*, International Particle Accelerator Conference No. 7 (JACoW, Geneva, Switzerland, 2016), pp. 1284–1286.
- [52] N. Warr, J. Walle, M. Albers, F. Ames, B. Bastin, C. Bauer, V. Bildstein, A. Blazhev, S. Bönig, N. Bree, B. Bruyneel, P. Butler, J. Cederkäll, E. Clément, T. Cocolios, T. Davinson, H. de Witte, P. Delahaye, D. DiJulio, J. Diriken *et al.*, *Eur. Phys. J. A* **49**, 40 (2013).
- [53] A. Ostrowski, S. Cherubini, T. Davinson, D. Groombridge, A. Laird, A. Musumarra, A. Ninane, A. di Pietro, A. Shotter, and P. Woods, *Nucl. Instrum. Methods Phys. Res. A* **480**, 448 (2002).
- [54] T. Czosnyka, D. Cline, and C. Wu, *Bull. Am. Phys. Soc.* **28**, 745 (1982), [www.slac.stanford.edu/pubs/proc/pubs/proc98/proc98\\_745.pdf](http://www.slac.stanford.edu/pubs/proc/pubs/proc98/proc98_745.pdf).
- [55] D. Cline, *Annu. Rev. Nucl. Part. Sci.* **36**, 683 (1986).
- [56] A. Gottberg, T. Mendonca, R. Luis, J. Ramos, C. Seiffert, S. Cimmino, S. Marzari, B. Crepieux, V. Manea, R. Wolf, F. Wienholtz, S. Kreim, V. Fedosseev, B. Marsh, S. Rothe, P. Vaz, J. Marques, and T. Stora, *Nucl. Instrum. Methods Phys. Res. B* **336**, 143 (2014).
- [57] S. Rothe, T. Day Goodacre, D. Fedorov, V. Fedosseev, B. Marsh, P. Molkanov, R. Rossel, M. Seliverstov, M. Veinhard, and K. Wendt, *Nucl. Instrum. Methods Phys. Res. B* **376**, 91 (2016).
- [58] F. Wenander, *Nucl. Instrum. Methods Phys. Res. B* **266**, 4346 (2008).
- [59] M. Zielińska, L. Gaffney, K. Wrzosek-Lipska, E. Clément, T. Grahm, N. Kesteloot, P. Napiorkowski, J. Pakarinen, P. Van Duppen, and N. Warr, *Eur. Phys. J. A* **52**, 99 (2016).
- [60] N. Kesteloot, B. Bastin, L. Gaffney, K. Wrzosek-Lipska, K. Auranen, C. Bauer, M. Bender, V. Bildstein, A. Blazhev, S. Bönig, N. Bree, E. Clément, T. Cocolios, A. Damyanova, I. Darby, H. De Witte, D. DiJulio, J. Diriken, C. Fransen, J. García-Ramos *et al.*, *Phys. Rev. C* **92**, 054301 (2015).
- [61] M. Klintefjord, K. Hadyńska-Klęk, A. Görgen, C. Bauer, F. L. BelloGarrote, S. Bonig, B. Bounthong, A. Damyanova, J. P. Delaroche, V. Fedosseev, D. A. Fink, F. Giacompo, M. Girod, P. Hoff, N. Imai, W. Korten, A. C. Larsen, J. Libert, R. Lutter, B. A. Marsh *et al.*, *Phys. Rev. C* **93**, 054303 (2016).
- [62] C. Lim, R. Spear, M. Fewell, and G. Gyapong, *Nucl. Phys. A* **548**, 308 (1992).
- [63] J. A. Winger, J. C. Hill, F. K. Wohn, E. K. Warburton, R. L. Gill, A. Piotrowski, R. B. Schuhmann, and D. S. Brenner, *Phys. Rev. C* **42**, 954 (1990).
- [64] J. Van Roosbroeck, H. De Witte, M. Gorska, M. Huyse, K. Kruglov, D. Pauwels, J. C. Thomas, K. Van de Vel, P. Van Duppen, S. Franchoo, J. Cederkall, V. N. Fedoseyev, H. Fynbo, U. Georg, O. Jonsson, U. Köster, L. Weissman, W. F. Mueller, V. I. Mishin, D. Fedorov *et al.*, *Phys. Rev. C* **71**, 054307 (2005).
- [65] L. A. Currie, *Anal. Chem.* **40**, 586 (1968).
- [66] O. Kenn, K.-H. Speidel, R. Ernst, S. Schielke, S. Wagner, J. Gerber, P. Maier-Komor, and F. Nowacki, *Phys. Rev. C* **65**, 034308 (2002).
- [67] A. Chester, B. A. Brown, S. P. Burcher, M. P. Carpenter, J. J. Carroll, C. J. Chiara, P. A. Copp, B. P. Crider, J. T. Harke, D. E. M. Hoff, K. Kolos, S. N. Liddick, B. Longfellow, M. J. Mogannam, T. H. Ogunbaku, C. J. Prokop, D. Rhodes, A. L. Richard, O. A. Shehu, A. S. Tamashiro *et al.*, *Phys. Rev. C* **104**, 054314 (2021).
- [68] J. L. Tracy, J. A. Winger, B. C. Rasco, U. Silwal, D. P. Siwakoti, K. P. Rykaczewski, R. Grzywacz, J. C. Batchelder, C. R. Bingham, N. T. Brewer, L. Cartegni, A. A. Ciemny, A. Fijałkowska, C. J. Gross, C. Jost, M. Karny, K. Kolos, A. Korgul, W. Królas, Y. Liu *et al.*, *Phys. Rev. C* **98**, 034309 (2018).
- [69] J. Henderson, C. Y. Wu, J. Ash, B. A. Brown, P. C. Bender, R. Elder, B. Elman, A. Gade, M. Grinder, H. Iwasaki, B. Longfellow, T. Mijatovic, D. Rhodes, M. Spieker, and D. Weisshaar, *Phys. Rev. C* **99**, 054313 (2019).
- [70] T. Otsuka, M. Honma, T. Mizusaki, N. Shimizu, and Y. Utsuno, *Prog. Part. Nucl. Phys.* **47**, 319 (2001).
- [71] N. Shimizu, T. Abe, Y. Tsunoda, Y. Utsuno, T. Yoshida, T. Mizusaki, M. Honma, and T. Otsuka, *Prog. Theor. Exp. Phys.* (2012) 01A205.
- [72] J. J. Ressler, R. F. Casten, N. V. Zamfir, C. W. Beausang, R. B. Cakirli, H. Ai, H. Amro, M. A. Caprio, A. A. Hecht, A. Heinz, S. D. Langdown, E. A. McCutchan, D. A. Meyer, C. Plettner, P. H. Regan, M. J. S. Sciaccchitano, and A. D. Yamamoto, *Phys. Rev. C* **69**, 034317 (2004).

- [73] X. F. Yang, Y. Tsunoda, C. Babcock, J. Billowes, M. L. Bissell, K. Blaum, B. Cheal, K. T. Flanagan, R. F. GarciaRuiz, W. Gins, C. Gorges, L. K. Grob, H. Heylen, S. Kaufmann, M. Kowalska, J. Kramer, S. Malbrunot-Ettenauer, R. Neugart, G. Neyens, W. Nortershauser *et al.*, [Phys. Rev. C \*\*97\*\*, 044324 \(2018\)](#).
- [74] C. Song, Z. Li, D. Vretenar, and J. Meng, [Sci. China Phys. Mech. Astron. \*\*54\*\*, 222 \(2011\)](#).
- [75] N. J. Abu Awwad, H. Abusara, and S. Ahmad, [Phys. Rev. C \*\*101\*\*, 064322 \(2020\)](#).
- [76] D. D. Dao and F. Nowacki, [Phys. Rev. C \*\*105\*\*, 054314 \(2022\)](#).
- [77] A. Poves, F. Nowacki, and Y. Alhassid, [Phys. Rev. C \*\*101\*\*, 054307 \(2020\)](#).
- [78] W. K. Koo and L. J. Tassie, [J. Phys. G: Nucl. Phys. \*\*7\*\*, L63 \(1981\)](#).
- [79] R. Orlandi, D. Mücher, R. Raabe, A. Jungclaus, S. Pain, V. Bildstein, R. Chapman, G. de Angelis, J. Johansen, P. Van Duppen, A. Andreyev, S. Bottoni, T. Cocolios, H. De Witte, J. Diriken, J. Elseviers, F. Flavigny, L. Gaffney, R. Gernhäuser, A. Gottardo *et al.*, [Phys. Lett. B \*\*740\*\*, 298 \(2015\)](#).
- [80] X. F. Yang, C. Wraith, L. Xie, C. Babcock, J. Billowes, M. L. Bissell, K. Blaum, B. Cheal, K. T. Flanagan, R. F. GarciaRuiz, W. Gins, C. Gorges, L. K. Grob, H. Heylen, S. Kaufmann, M. Kowalska, J. Kraemer, S. Malbrunot-Ettenauer, R. Neugart, G. Neyens *et al.*, [Phys. Rev. Lett. \*\*116\*\*, 182502 \(2016\)](#).